High bandwidth optical coherent transient true-time delay
by Randy Ray Reibel

A dissertation submitted in partial fulfillment of the requirements for the degree of Doctor of Philosophy in Physics
Montana State University

Abstract:
An approach to reaching high bandwidth optical coherent transient (OCT) truetime delay (TTD) is described and demonstrated in this thesis. Utilizing the stimulated photon echo process in rare-earth ion doped crystals, such as Tm3+:YAG, TTD of optical signals with bandwidths > 20 GHz and high time bandwidth products > 104 are possible. TTD regenerators using OCT's have been demonstrated at low band-widths (< 40 MHz) showing picosecond delay resolutions with microsecond delays. With the advent of high bandwidth chirped lasers and high bandwidth electro-optic phase modulators, OCT TTD of broadband optical signals is now possible in the multi-gigahertz regime.

To achieve this goal, several theoretical and technical aspects had to be explored. Theoretical discussions and numerical simulations are given using the Maxwell-Bloch equations with arbitrary phase. These simulations show good signal fidelity and high (60%) power efficiencies on echoes produced from gratings programmed with linear frequency chirps. New approaches for programming spectral gratings were also examined that utilized high bandwidth electro-optic modulators. In this technique, the phase modulation sidebands on an optical carrier are linearly chirped, creating an analog to the common linear frequency chirp. This approach allows multi-gigahertz true-time delay spectral grating programming. These new programming approaches are examined and characterized, both through simulation and experiment.

A high bandwidth injection locked amplifier, based on semiconductor diode lasers, had to be developed and characterized to boost optical powers from both electro-optic phase modulators as well as chirped lasers. The injection locking system in conjunction with acousto-optic modulators were used in high bandwidth TTD demonstrations in Tm3+:YAG. Ultimately, high bandwidth binary phase shift keyed probe pulses were used in a demonstration of broadband true-time delay at a data rate of 1 GBit/s. The techniques, theory, and demonstrations described in this thesis can also be applied to high bandwidth optical signal processing and arbitrary waveform generation using optical coherent transient phenomena.

HIGH BANDWIDTH OPTICAL COHERENT TRANSIENT TRUE-TIME DELAY

by

Randy Ray Reibel

A dissertation submitted in partial fulfillment
of the requirements for the degree

of

Doctor of Philosophy

in

Physics

MONTANA STATE UNIVERSITY
Bozeman, Montana

May 2002

APPROVAL

of a dissertation submitted by

Randy Ray Reibel

This dissertation has been read by each member of the dissertation committee and has been found to be satisfactory regarding content, English usage, format, citations, bibliographic style, and consistency, and is ready for submission to the College of Graduate Studies.

Wm. Randall Babbitt _____ 5/13/02
(Signature) Date

Approved for the Department of Physics

John C. Hermanson _____ 5-13-02
(Signature) Date

Approved for the College of Graduate Studies

Bruce R. McLeod _____ 5-21-02
(Signature) Date

STATEMENT OF PERMISSION TO USE

In presenting this dissertation in partial fulfillment of the requirements for a doctoral degree at Montana State University, I agree that the Library shall make it available to borrowers under rules of the Library. I further agree that copying of this dissertation is allowable only for scholarly purposes, consistent with "fair use" as prescribed in the U. S. Copyright Law. Requests for extensive copying or reproduction of this dissertation should be referred to Bell & Howell Information and Learning, 300 North Zeeb Road, Ann Arbor, Michigan 48106, to whom I have granted "the exclusive right to reproduce and distribute my dissertation in and from microform along with the non-exclusive right to reproduce and distribute my abstract in any format in whole or in part."

Signature R. Bell

Date 5/13/02

ACKNOWLEDGEMENTS

This dissertation could not have happened without the help of so many people. First, let me thank my advisor, Dr. W. Randy Babbitt, for allowing me the opportunity to be a part of this challenging research project. Dr. Babbitt's fundamental grasp on OCT's and his ability to teach others are the main reasons this dissertation even exists. Randy, thank you for your years of kindness, support, and smiles.

I want to thank Dr. Mingzhen Tian, the Research Scientist in our group. Without her encouragement, instruction and leadership this thesis would not exist. Mingzhen, thanks for listening to me, answering my questions, and staying awake during those late hours in the lab.

I want to thank all my fellow group members. I need to give special thanks to Zeb Barber for his outstanding help and also his wonderful friendship. To Zhiqiang Jia, without whose help the injection locking simulator would not exist. Thanks to Spectrum Lab employees Zachary Cole and Kris Merkel for their constant help, frisbee golf, and unique perspectives on life. I want to also thank Pete Roos, for his friendship, answers, and memories climbing.

Finally, love and thanks to all of my family. To my wife Sandra Lynn, for your incredible, unbelievable support, strength and sacrifice through these years. Your love inspires and captures me. To Ransom for insisting I play once in a while. And to Maggie for her wagging tail and midnight walks.

TABLE OF CONTENTS

LIST OF TABLES

LIST OF FIGURES

ABSTRACT

An approach to reaching high bandwidth optical coherent transient (OCT) true-time delay (TTD) is described and demonstrated in this thesis. Utilizing the stimulated photon echo process in rare-earth ion doped crystals, such as Tm^{3+}:YAG, TTD of optical signals with bandwidths > 20 GHz and high time bandwidth products $> 10^4$ are possible. TTD regenerators using OCT's have been demonstrated at low bandwidths (< 40 MHz) showing picosecond delay resolutions with microsecond delays. With the advent of high bandwidth chirped lasers and high bandwidth electro-optic phase modulators, OCT TTD of broadband optical signals is now possible in the multi-gigahertz regime.

To achieve this goal, several theoretical and technical aspects had to be explored. Theoretical discussions and numerical simulations are given using the Maxwell-Bloch equations with arbitrary phase. These simulations show good signal fidelity and high (60%) power efficiencies on echoes produced from gratings programmed with linear frequency chirps. New approaches for programming spectral gratings were also examined that utilized high bandwidth electro-optic modulators. In this technique, the phase modulation sidebands on an optical carrier are linearly chirped, creating an analog to the common linear frequency chirp. This approach allows multi-gigahertz true-time delay spectral grating programming. These new programming approaches are examined and characterized, both through simulation and experiment.

A high bandwidth injection locked amplifier, based on semiconductor diode lasers, had to be developed and characterized to boost optical powers from both electro-optic phase modulators as well as chirped lasers. The injection locking system in conjunction with acousto-optic modulators were used in high bandwidth TTD demonstrations in Tm^{3+}:YAG. Ultimately, high bandwidth binary phase shift keyed probe pulses were used in a demonstration of broadband true-time delay at a data rate of 1 GBit/s. The techniques, theory, and demonstrations described in this thesis can also be applied to high bandwidth optical signal processing and arbitrary waveform generation using optical coherent transient phenomena.

CHAPTER 1

INTRODUCTION TO HIGH BANDWIDTH OPTICAL COHERENT TRANSIENTS

The goal of this thesis is to describe and demonstrate an approach to reaching high bandwidth optical coherent transient (OCT) true-time delay. True-time delay (TTD) is useful in a number of potential applications including phased array antenna systems, arbitrary waveform generation and correlators. This chapter presents an introduction to this research topic including a brief overview of stimulated photon echoes (SPE). The potential usefulness of photon echoes in these high bandwidth systems is examined and an overview of how to reach these bandwidths is shown. An overall description and the organization of this thesis is also given.

Introduction To Research Topic

In Merriam-Webster's Online Collegiate Dictionary the word echo has the definition: *the repetition of a sound caused by reflection of sound waves* [1]. Most all of us are familiar with the effect of an acoustic or reflection echo. Whether we were in a large auditorium, outside near a building or inside some room, an echo is the repetition of our words caused by a reflection of the sound waves from some surface. Echoes are unique in that they mimic or repeat the words of the person who uttered them although often the echo is fainter or a less intense sound. The amount of time

it takes before an echo reaches an observer is directly proportional to the distance the observer is from the surface that has reflected the sound. Thus by changing the distance to the reflecting surface an echo's time delay can be varied. In much the same way, a photon echo, generated from an OCT process, follows these traits, however, the waveform is no longer an acoustic wave but an electromagnetic wave. The photon echo is not created by reflection from a surface, it is instead created by a complex physical process in an optically absorbing material. In certain situations the photon echo waveform will exactly mimic the original electromagnetic waveform, however with less intensity and a variable time delay. These characteristics are similar to the acoustic echo and are what gives rise to the name *photon echo*. But the photon echo is much more than a simple reflection from a surface and the OCT processes that govern it are truly unique and can be used as a powerful optical processing tool for a variety of applications.

One such application for the photon echo is as a component that can control, steer and adaptively beamform phased array antennas. Phased array antennas, steered with conventional electronics, currently perform a variety of tasks and find application to both military and civilian markets. These systems make use of the wavelike properties of electromagnetic radiation to "steer" beams without ever physically moving the antenna. The significant benefits of such systems over conventional radar systems were quickly noticed and several phased array radar systems became operational in the 1960's [2]. The operational premise of such a system is shown in figure 1. These

arrays can be used to transmit or receive a variety of waveforms. The array antenna is a collection of RF emitters, each emitting its individual electromagnetic field. In the far field, the electromagnetic fields of each emitter sum to form the overall beam pattern from the antenna array.

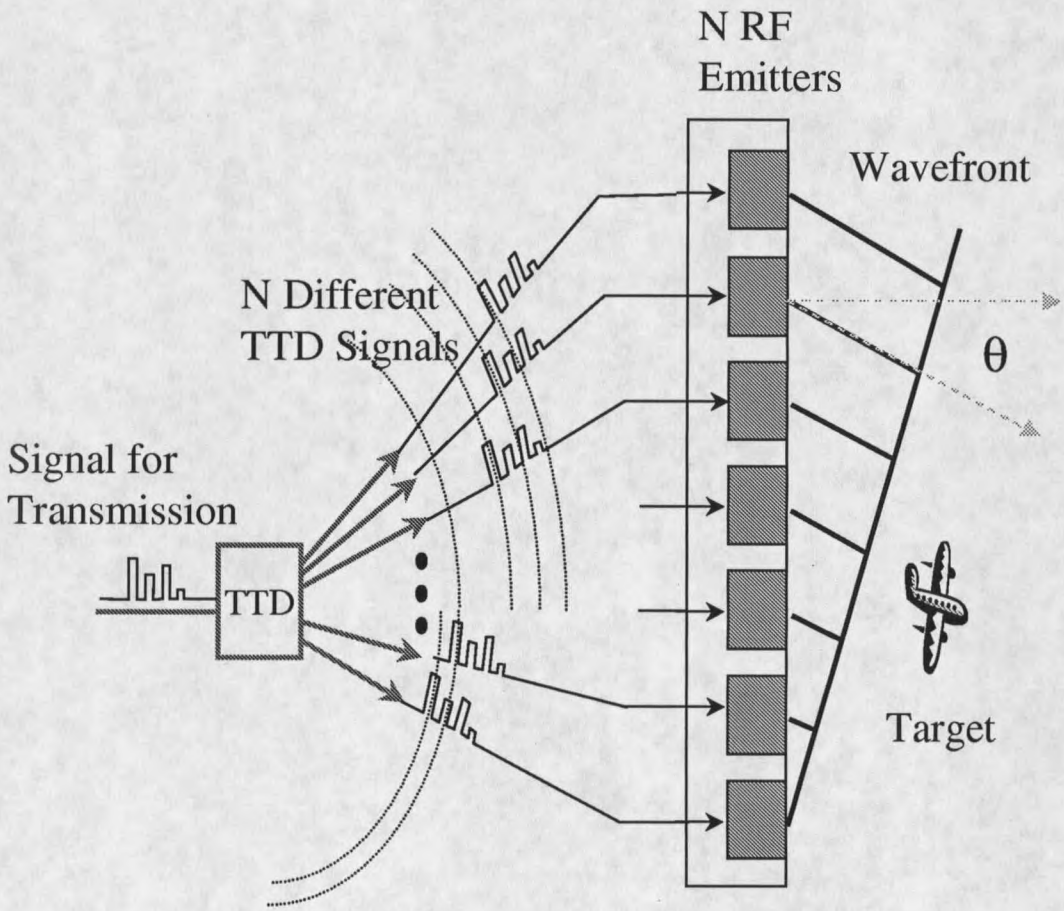

Figure 1. The operational design of how a phased array system works.

This overall beam pattern in the far field is known as the antenna beam lobe. This lobe can be controlled or steered utilizing the wave-nature of electromagnetic fields. If the time delay from each emitter to a spatial location away from the array can be controlled, the signal at that spatial location can be made to constructively or destructively interfere with the field produced at that location from other emitters. In the far field, the delay imparted to the electromagnetic fields from each emitter allows the beam lobe to be steered as shown in figure 1. Thus, the time delay of the electrical signals becomes the key component to the operation of a phased array radar. In narrow band (nearly single frequency) antenna arrays, the time delay of an electrical signal need not be *true* time delay. Instead, the electrical signal can be simply phase shifted. A single frequency sinusoidal waveform that is phase shifted is equivalent to one that is time delayed. Thus, simple electronic phase shifting devices could be used to steer the antenna, assuming the waveform is close to a single frequency sinusoidal waveform (narrow band) or, in other words, has a low fractional bandwidth (bandwidth divided by carrier). As the bandwidth deviates from narrowband an equal phase shift no longer translates directly to an equal time delay of the whole waveform. Essentially, different frequency components getting the same phase shift from the phase shifter, have a time delay, τ_D, that can be written as

$$\tau_D(\omega_m) = \phi/\omega_m. \tag{1.1}$$

Here ϕ is the constant phase shift imparted by the phase shifting device, and ω_m is

a frequency component of the broadband signal. If the fractional bandwidth of the signal is large, one can see that different ω_m's will experience different time delays, τ_D. This causes signals with significant bandwidths to behave improperly when steered with phase shifting devices. This imparts what is known as beam squint on the main lobe of the radiation field emitted from the array elements. Since delay and angle are related in a phased array, beam squint essentially means the steering of different frequency components of the signal into different angular directions. This angular spread, $\Delta\theta$, is given by

$$\Delta\theta = -\frac{B}{\omega_{RF}}\tan(\theta) \tag{1.2}$$

Here, B is the bandwidth of the signal, ω_{RF} is the carrier frequency of the radar (giving a fractional bandwidth B/ω_{RF}), and θ is the steering angle of the main lobe [3]. As can be seen, the angular deviation is a linear function of the fractional bandwidth, giving large angular deviations of frequency components for large fractional bandwidths. It should be noted that the angular size of the antenna beam lobe gets smaller with more antenna elements. Thus, if a large phased array radar (with high fractional bandwidths) uses phase shifters to control the time delay, beam squint will be a significant problem [4].

In order for a system of antenna elements to properly steer signals with large fractional bandwidths, the elements must impart a true-time delay (TTD) on the signals. TTD means that each frequency component of the signal for a given emitter gets the same time delay rather than the same phase shift. Thus, eqn. (1.1) can be

rearranged as

$$\phi(\omega_m) = \omega_m \tau_D. \tag{1.3}$$

In a TTD system it is τ_D that typically remains constant (per element), and thus the phase shift needed will change according to the given frequency component, ω_m. Producing broadband TTD waveforms is the main emphasis of this thesis.

There have been many proposals for optical TTD control of an RF signal. These include but are not limited to delaying optical signals via different optical delay lines or creating delays by frequency shifting the optical carrier in a highly dispersive optical fiber [3]. In the first approach, several different techniques have been envisioned but all follow the same principle. That principle is that one would choose the time delay for the optical signal by switching the optical pulse into an appropriate delay line. One suggestion is to use several different length optical fibers to give various different delays. Unfortunately, as the number of array elements grows, the switching network for such a system becomes increasingly complex as does the amount of fiber needed. For the second approach, simply by changing the frequency of the optical carrier a different delay can be chosen because the index of refraction for that frequency has changed. In this case, it is the number of distinctive frequency channels that can be achieved by the optical source that limits the resolution of the delays to less than 1 part in 1000 [3]. Along with this, a tunable diode laser and fiber must be used for each element of the array. Again, this results in an increasing complexity and cost as the number of array elements is increased. These systems also have no ability to

control the phase, number, or weight of these delays, and thus adaptive beamforming or jammer nulling can not be done with such systems.

It has been suggested that the SPE process can be used to create the TTD needed to avoid beam squint in a phased array radar or communication system [5]. Instead of using an electronic phase shifter, the photon echo would be used to create TTD. The properties of OCT's are such that the photon echo can theoretically delay signals with tens of gigahertz bandwidths over delays of microseconds with picosecond resolutions. The delays can be programmed on the fly or preprogrammed. The storage capabilities of OCT's enable several different delays to be stored spatially in the OCT medium providing more than a million different delays all within a single compact crystal. This along with the ability to individually control the delay of each frequency component makes OCT's an attractive basis for steering a phased array antenna, especially ones requiring adaptive beamforming and jammer nulling.

In order to create a stimulated photon echo, an inhomogeneously broadened absorber (IBA), such as a rare-earth ion doped crystal, is used. Because of the special properties of IBA's, a time delay between two incident brief programming pulses is stored as a spectral grating within the medium. This grating can be probed sometime later by another incident brief pulse. The medium is then coherently stimulated and produces a stimulated photon echo with the delay that was stored in the spectral grating. In the linear regime, this process is not limited to just temporally brief probe pulses. Any arbitrarily shaped incident probe pulse can be delayed assuming

the bandwidth of the spectral grating is larger than the bandwidth of the probe.

OCT's have previously been demonstrated as TTD devices giving microsecond delay times and picosecond resolutions [6]. Various methods including brief pulse programming and chirped pulse programming have been explored to produce TTD spectral gratings [7]. However, almost all previous demonstrations were over a limited bandwidth (typically 40 MHz) and did not reach the ideal goal of showing TTD with multi-gigahertz bandwidths. This thesis extends TTD demonstrations to the gigahertz bandwidth, along with developing more practical OCT techniques to program multi-gigahertz TTD.

Programming and probing broadband spectral gratings is not an easy task. In order to program an efficient spectral grating, a significant amount of optical energy must be transferred to the medium. Unfortunately, if brief pulses are used to program these broadband gratings, their temporal lengths must be extremely short (on the order of 100 picoseconds) to achieve large bandwidths. Producing these types of brief pulses is not easy, requiring the use of mode-locked lasers with amplification. These systems are impractical because of their cost, power inefficiencies and size. And, even though powerful pulsed lasers exist with tremendous power per pulse (~GW), producing efficient broadband spectral gratings with these lasers has proven challenging. The intensities required are near or exceed the damage threshold of OCT crystals. Processes such as accumulation of spectral gratings, where less powerful programming pulses are repeatedly applied to the medium, must be used in order to produce

efficient gratings.

Another way to produce a spectral grating in an OCT media is through the use of linear frequency chirped pulses [7]. Linear frequency chirps (LFC's) ramp their instantaneous frequency linearly as a function of time. Through the proper choice of chirp bandwidth and chirp duration, a power limited laser can program much more efficient TTD spectral gratings, as compared to brief pulses from the same laser. High bandwidth (> 20 GHz) LFC's are now a possibility due to the recent advances in chirped external cavity diode lasers (CECDL's) [8, 9].

Broadband signals are also inherently harder to detect because of noise issues. The level of thermal noise detected increases as the square root of the bandwidth. Thus, this thermal noise limits the detection of broadband echoes. Poor echo efficiencies also contribute to these detection problems. Recently, photon echoes with greater than unit efficiency have been suggested and observed for certain situations using optically thick samples [10, 11]. Unfortunately, the direct results from these research efforts are not applicable to TTD. This thesis examines the efficiencies of photon echoes for the situation of TTD for both brief pulse programming and LFC programming in optically thick crystals. Another problem is that these broadband RF signals must be imparted to the optical carrier, TTD, and subsequently converted to RF signals. The TTD optical signals must be detected in a fashion that allows detection of the encoded broadband signals. Various methods of modulation and detection are explored. It is also shown that the spectral grating itself can be utilized in making more efficient

detection methods for optically encoded broadband signals.

Another reason previous demonstrations were limited to low bandwidths (40 MHz) was the lack of suitable high bandwidth modulators to create probe signals. Advancements in high bandwidth, affordable electro-optic modulators (EOM's) makes the encoding of high bandwidth electronic signals onto optical carriers easier. Unfortunately, at the wavelength with which most of our work is done (793 nm) these EOM's are optical power limited due to photorefractive damage. The maximum output powers are 1 to 2 orders of magnitude lower than that required to produce detectable broadband photon echoes. In order to overcome this power limitation, a suitable amplifier for high bandwidth signals was developed using EOM's and an injection locked amplifier.

Overview of Thesis

This thesis details the possible approaches for creating high bandwidth TTD along with the problems and solutions. As stated above TTD applications such as phased array radars and communication systems will benefit from this research. But, as with any type of science, there are other unexpected benefits from the research and other applications to which this research can be applied. The desire to bring OCT's into the high bandwidth regime is a continuing struggle, one that is ongoing with new developments and twists everyday. This thesis is a snapshot of the past three years detailing the steps and barriers that had to be overcome before high bandwidth TTD

could be realized. What follows is a brief description of the chapters found within this thesis.

In chapter 2, the theoretical framework needed for this thesis is developed and presented. This includes a detailed overview of the stimulated photon echo process and the linear filter theory that predicts the dynamics of this process in certain regimes. An outline of other approaches to predictive solutions is given for various conditions. Chapter 2 also includes a discussion on the Maxwell-Bloch equations including arbitrary phases of the field. This mathematical approach, combined with simulation, allows quantitative predictions of the OCT phenomena covered in this thesis. Specifically, high efficiency TTD is studied for thick crystals utilizing linear frequency and linear phase chirps. Aspects such as delay resolution and signal fidelity are also examined with this simulator.

Chapter 3 presents the important practical considerations for reaching high bandwidth TTD using the stimulated photon echo process. A discussion of phase modulated signals created from high bandwidth EOM's is given. Spectral filtering effects caused by the medium as well as programmed spectral gratings are examined for these high bandwidth signals. It is shown that detection schemes utilizing these spectral filters can be more efficient than conventional detection schemes. Experimental parameters and material details are discussed as well as problems related to temporally long probe pulses. Simulations are performed for optically thick samples, showing that expected echo efficiencies using chirped programming can reach 60%.

The chapter also examines the aspects of accumulation and continuous programming and continuous processing, which are relevant to this thesis.

Chapter 4 shows how to amplify broadband signals from the power limited EOM's using an injection locking system. The needed theoretical framework for injection locking is detailed as well as experimental demonstrations of the amplifier. The benefits of such a system include ease of use and gains of more than 20 dB. However, using injection locking with semiconductor diode lasers has inherent challenges that will be discussed.

Through experimental demonstrations, problems related to high bandwidth linear frequency chirped programming were uncovered that called for modifying the previous approach to linear frequency chirp programming. Chapter 5 presents the modification of the linear frequency chirped programming method. The modification was to temporally overlap two frequency offset linear frequency chirps. Both low bandwidth demonstrations and high bandwidth demonstrations (using a CECDL) are presented. The tuning linearity of this method is examined as well as the efficiency of programmed gratings for TTD versus bandwidth scaling. Results from accumulation using this new method are also presented.

Finally, a novel technique for programming TTD gratings into an OCT medium using the broadband EOM's is presented in chapter 6. By using an EOM in conjunction with the injection locked amplifier, one can create multi-gigahertz gratings in the OCT media. This novel technique relies upon linear sideband chirping (LSC) and in

chapter 6 this approach is detailed. Experimental TTD results of both data and CW waveforms, which are delayed over several hundreds of nanoseconds, are presented. Data rates of 1 Gbit/s and bandwidths of 1 GHz are achieved. The tuning linearity and the resolution of this method are also analyzed.

CHAPTER 2

THEORETICAL OVERVIEW OF OPTICAL COHERENT TRANSIENTS

A basic overview of OCT's followed by the development of the coupled Maxwell-Bloch equations is given in this chapter. The basic operation of OCT's in the linear regime (energetically weak pulses) can be understood from a simple conceptual framework using a Fourier transform approach. In optically thin media, one can invoke the undepleted pump approximation that assumes the output electric field is proportional to the polarization of the thin medium. Using this approximation, the output electric field is a linear transform of the input pulses. While this is useful in describing the output from the medium, the assumptions invoked mean working in a regime of poor power efficiencies. By including the effects of propagation, where the polarization acts back on the field, highly efficient photon echoes can be created in optically thick media [10, 12, 13, 11]. To do this, the Maxwell wave equation must be used in conjunction with the optical Bloch equations that describe the dynamics of the medium. Expressions that can be solved analytically for certain cases have been shown [13] for the coupled Maxwell-Bloch equations (assuming energetically weak pulses or temporally brief pulses). The analytic solutions found were compared with direct numerical integrations of the Maxwell-Bloch equations and were found to be in good agreement [13]. However, the previous approaches to solving the propagation

effects of the medium did not allow for arbitrary phase and frequency for the input pulses [10, 12, 13]. The phase can not be ignored for pulses that are linearly chirped such as those used in this thesis. Here, a derivation for the Maxwell-Bloch equations is given for arbitrary phase and frequency. These equations are then used as the basis for a Maxwell-Bloch simulator that can predict the output of pulses with arbitrary phase and frequency in an optically thick regime. This allows analysis of the echo power efficiency for linear frequency chirped programming pulses.

Optical Coherent Transients And The Photon Echo

Properties Of OCT Media

In order to begin a discussion on the photon echo, it helps to understand some of the basic properties of the medium in which photon echoes can take place. Photon echoes have been observed in various kinds of media ranging from inorganic rare-earth-ion-doped crystals, such as Tm^{3+}:YAG [14], to gases of heated materials, such as barium or sodium heated in an oven [15], and even to amorphous systems of large organic molecules [16]. All of these materials, as varied as their physical makeup is, contain similar physical properties, which allow them to produce the photon echo.

First, like any optical phenomena, there must be an optical transition between two atomic levels in the material of interest. This allows a given atom within the medium to become excited, by absorbing a photon. Once an atom is in an excited state, it can leave the excited state through either spontaneous emission or stimulated

emission. The spontaneous emission decay rate Γ_e, gives rise to an exponential decay of the upper state with lifetime, $T_1 = 1/2\pi\Gamma_e$. The upper state lifetime is important in the photon echo process, as it determines the lifetime of the upper state spectral grating.

For the photon echo process, there is a fundamental limit to the amount of time delay that can be created. This limit arises due to the coherence lifetime or irreversible dephasing time in the crystal. This lifetime is given as $T_2 = 1/\pi\Gamma_H$, where Γ_H is the homogeneous linewidth. In an inorganic crystal, this individual atomic linewidth is created due to perturbations such as lattice phonon coupling, nuclear and electron spin couplings as well as the overall population decay rate. It is known as the "homogeneous" linewidth because the broadening is experienced equally by all atoms within the medium. For demonstrations in Tm^{3+}:YAG, Γ_H is mostly dominated by phonon coupling and is thus heavily dependent upon temperature [17]. Typical homogeneous linewidths for rare-earth ion doped crystals used in this thesis are tens of kilohertz, but have been measured to be as narrow as 122 Hz [18].

Another broadening mechanism, called inhomogeneous broadening, exists within these crystals. Due to imperfections within a rare-earth ion doped crystal, the local environment of a given ion can be perturbed resulting in a different resonant frequency for the ion. Since the perturbations add randomly, the inhomogeneous line typically has a Guassian lineshape. Because the inhomogeneous broadening plays such a critical role in OCT phenomena these materials are often referred to as inhomogeneously

broadened absorbers (IBA's).

An OCT medium is effectively a frequency selective absorber of optical energy. To first order (weak intensities), interaction of the medium with the optical field is known as Beer's Law and the intensity, I, of the light at a given point in the medium is given by [19]

$$I = I_o e^{-\alpha z}. \tag{2.1}$$

Here, I_o, represents the intensity of the input electric field (z=0), z is the coordinate of propagation in the medium, and α is known as the absorption coefficient. Because the amount of light absorbed from the transmitted field depends upon the interaction length, L, a particular crystal can be described by the unitless parameter known as the absorption length, αL. The absorption length is an important parameter. The smaller αL is the less important propagation effects become, allowing them to be ignored for small enough αL (undepleted pump approximation). However, for αL on the order of 1, propagation effects become apparent and must be included in a full analysis of the system.

Spectral Hole Burning

In a crystal with a large inhomogeneous linewidth, the ions within Γ_H of each other can be accessed by a narrowband laser without disturbing the other ions within the inhomogeneous linewidth. A laser, tuned to a specific energy within the inhomogeneous band, excites ions with that frequency to the excited state and burns a hole

in the ground state population. Figure 2 (a) shows the Guassian shaped inhomogeneously broadened transition of width Γ_I being made up of individual Lorentzian lines with width Γ_H, each of which represent a collection of ions with equal transition frequencies (within $\pm\Gamma_H/2$). In figure 2 (b), both the ground state population and the excited state population are shown after a narrowband laser with frequency f_L illuminates the crystal.

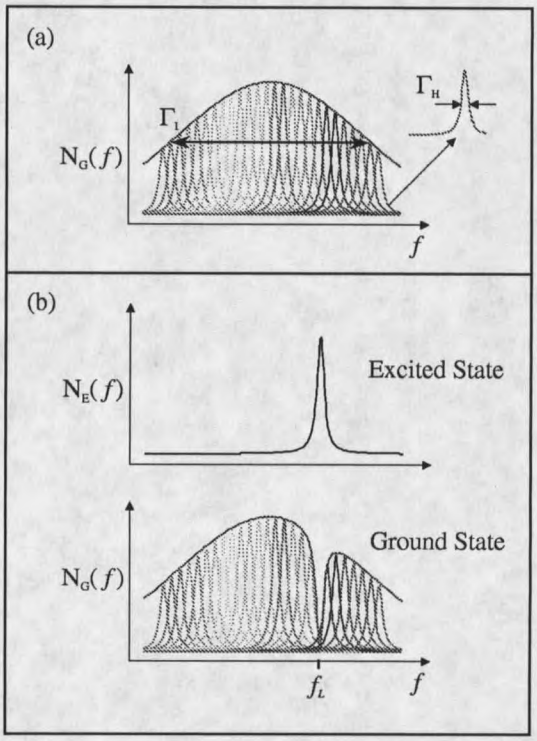

Figure 2. (a) Shows a typical Guassian shaped inhomogeneously broadened transition made up of individual Lorentzian lines from atoms at different frequencies. (b) The transition after being illuminated by a laser with frequency f_L. The lower trace shows a hole in the transition, where the electrons have been transferred to the excited state, upper trace.

This process is known as spectral hole burning. Essentially, a hole is created in the absorption band of the medium at a specific frequency. Hole burning has been put forward as a possible way to store information and has been studied extensively in various types of media [20]. Theoretically, the number of holes that can be burned into an ideal IBA medium is Γ_I/Γ_H and is often referred to as the time-bandwidth product (TBP) of the IBA. TBP's from $10^4 - 10^8$ are possible in rare-earth ion doped crystals [18]. Though practical limitations will likely keep the upper limit of the TBP to be less than 10^6.

Spectral Gratings and The Photon Echo

In 1964, N. A. Kurnit, I. D. Abella and S. R. Hartmann made the first observation of photon echoes [21]. Figure 3 shows two types of photon echoes; the two pulse photon echo, 2PE, and the stimulated photon echo, SPE. This figure shows the first two pulses, P_1 and P_2. They are separated by a time delay, $\tau_{21} = t_2 - t_1$. Here t_i indicates the arrival time at the front of the medium for the i'th pulse. At a time τ_{21} after the second pulse, the 2PE occurs. Essentially P_1 creates coherences within the medium. These coherences begin to dephase with respect to each other due to their individual atomic frequencies. Then P_2 acts on the medium and flips the phases of these coherences. The coherences then begin to rephase and at τ_{21} after P_2 produce the 2PE.

If another pulse of light is incident upon the medium after P_1 and P_2, such as

P_3, another echo, the SPE, occurs at τ_{21} after P_3. In this figure, the temporal pulse widths were $\tau_p = 100$ ns and $\tau_{21} = 1100$ ns. The first two pulses, P_1 and P_2, will be referred to as the programming pulses, because they program the time delay, τ_{21}, into the medium, and P_3 is the probe pulse.

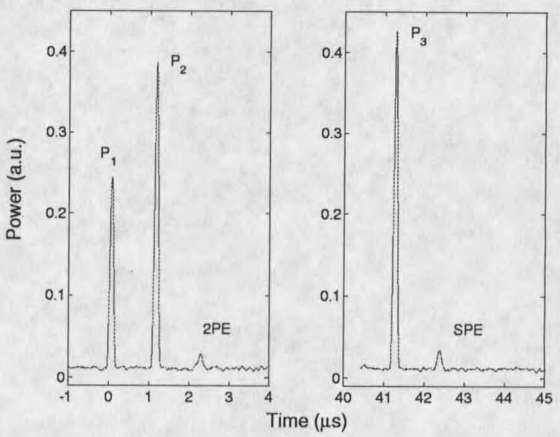

Figure 3. Experimental demonstration of the two pulse photon echo (2PE) and the stimulated photon echo (SPE). In this figure, the temporal pulse widths were $\tau_p = 100$ ns and $\tau_{21} = 1100$ ns. Experiment performed by the author.

As was stated above, the OCT medium has the ability to record the frequency information of incident light pulses. This happens because the light coherently excites the atoms from the ground state into the excited state. The spectral distribution of the pulse contains more energy in certain frequencies than in others. Those frequencies with more energy tend to excite more atoms, whereas those with less energy excite less atoms. This process has the effect of imprinting the spectral distribution of the pulse into the relative atomic populations of the medium. Thus energy has been transferred from the pulse to the medium. The OCT medium can be thought of as

a storage system for the power spectrum of the programming sequence, P_1 and P_2. After programming, this absorption spectrum acts as a linear frequency-domain filter on any other input pulses, assuming certain conditions are met. It is assumed that the pulses are energetically weak. The pulse area, Θ, of a pulse, is defined as

$$\Theta = \frac{\mu_{12}}{\hbar} \int E_o(t)dt \; . \tag{2.2}$$

Here μ_{12} is the dipole moment and E_o is the slowly varying envelope of the electric field. If a pulse is energetically weak, the pulse area is small ($\Theta \ll 1$). Along with this, the system is taken to be optically thin ($\alpha L \ll 1$), allowing the undepleted pump approximation. With these assumptions, the output from the OCT system follows linear filter theory.

Under the linear filter theory, the output of the system is a combination of the input response, f(t), with how the system was programmed, h(t). In the case described above, the system was programmed with two incident optical pulses. The inhomogeneously broadened crystal stores the power spectrum of these combined pulses provided $\tau_{21} < T_2$. If the incident optical fields are defined by $E_1(t)$ and $E_2(t)$, the power spectrum of these two pulses is

$$\tilde{H}(\omega) = |\tilde{E}_1(\omega)|^2 + |\tilde{E}_2(\omega)|^2 + \tilde{E}_1{}^*(\omega)\tilde{E}_2(\omega) + \tilde{E}_1(\omega)\tilde{E}_2{}^*(\omega) \; . \tag{2.3}$$

Here $\tilde{E}_i(\omega)$ represents the electric field of the i'th pulse in the frequency domain. The first two terms are the power spectra of just the individual pulses themselves. The third and fourth terms represent the spectral interference of the two pulses. These

two terms are analogous to the interference terms encountered in spatial holography. The important contribution from the power spectrum to the stimulated photon echo is the first cross term and thus the power spectrum is rewritten as

$$\tilde{H}(\omega) = \tilde{E_1}^*(\omega)\tilde{E_2}(\omega) , \tag{2.4}$$

where the other terms are ignored. In the linear filter theory, $\tilde{H}(\omega)$ is known as the frequency-domain response function. The Fourier transform of a function is defined as

$$\tilde{F}(\omega) = \frac{1}{\sqrt{2\pi}} \int_{-\infty}^{\infty} f(t)\, e^{i\omega t}\, dt . \tag{2.5}$$

In subsequent sections the Fourier transform can be identified by the "ω" in the argument. The inverse Fourier transform is then

$$f(t) = \frac{1}{\sqrt{2\pi}} \int_{-\infty}^{\infty} \tilde{F}(\omega)\, e^{-i\omega t} d\omega . \tag{2.6}$$

In the linear filter theory, the output from the programmed system, defined $g(t)$, is related to the input of the system, $f(t)$, by the relation

$$g(t) = \int_{-\infty}^{\infty} h(t-\tau) f(\tau)\, d\tau . \tag{2.7}$$

The function $h(t)$ is called the time-domain response function. The function, $f(t)$, represents the third optical pulse, $E_3(t)$ (or other subsequent pulses), incident upon the OCT medium. The function, $g(t)$, can be examined in the frequency-domain by taking the Fourier transform giving

$$\tilde{G}(\omega) = \tilde{H}(\omega)\, \tilde{F}(\omega) . \tag{2.8}$$

Now the system's response to the third pulse, $\tilde{F}(\omega) = \tilde{E}_3(\omega)$, can be written in the frequency domain as

$$\tilde{E}_{out}(\omega) \propto \tilde{E}_1{}^*(\omega)\tilde{E}_2(\omega)\tilde{E}_3(\omega) \ . \tag{2.9}$$

If the two programming pulse envelopes are Guassian in nature, the Fourier transform of each individual pulse is itself a Guassian envelope in the frequency-domain. There is a time shift between these two Guassian input pulses, τ_{21}. Because of this time delay, the Fourier transform of the second pulse includes a linear phase shift with respect to the Fourier transform of the first pulse, that is dependent upon the frequency and time delay, $e^{-i\omega\tau_{21}}$. This linear phase shift gives rise to a modulation in the power spectrum and thus a spectral grating in the medium with a period of $1/\tau_{21}$. Much like spatial gratings, which can act to diffract pulses in the spatial domain, a spectral grating can diffract a pulse in the time domain. If the period of a spatial grating is tuned, the angular output for an incident wavelength is changed. If the period of a spectral grating is tuned, the time delay of the output is changed.

In figure 4 (a) the electric field of two programming pulses are shown with $\tau_{21} =$ 10 ns. In order to simulate the output from the above linear analysis, the electric field must be oscillating much faster than the slowly varying envelope of the optical pulse. This essentially means that the pulse's bandwidth is much less than the carrier frequency. Here the total power spectrum is simulated so effects due to both spectral interference terms in eqn. (2.3) are included.

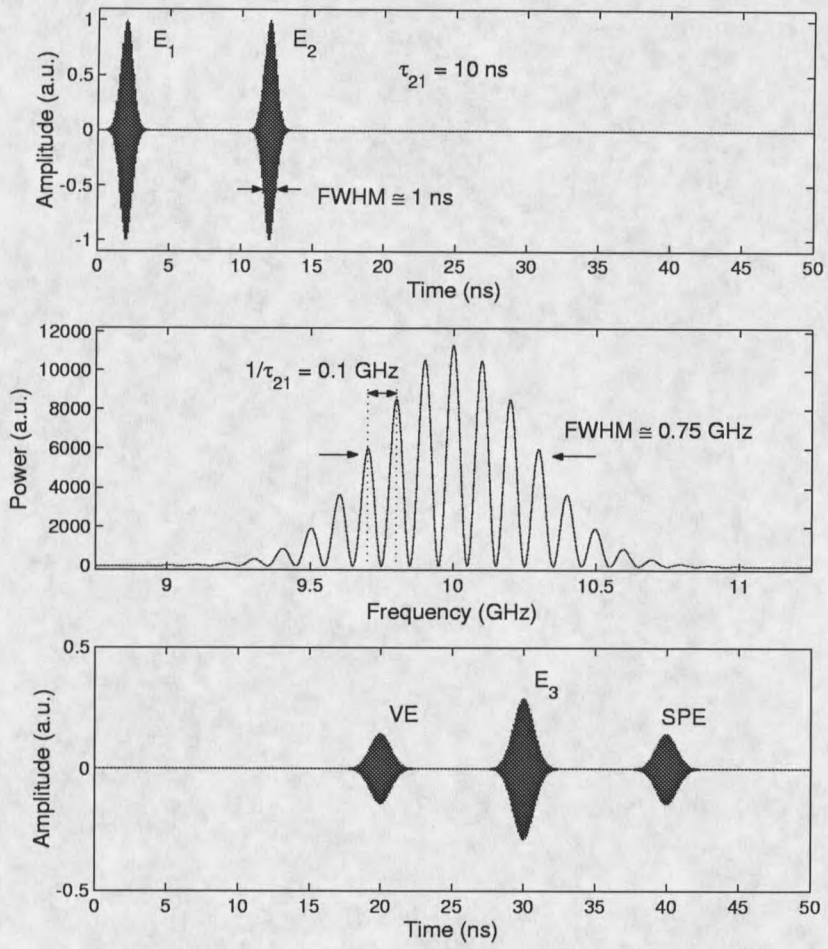

Figure 4. (a) Shows the two programming pulses, FWHM $\approx$ 1 ns, $\tau_{21} = 10$ ns. (b) Shows the resulting power spectrum. (c) The expected output as calculated using non-causal linear filter theory. One can see the SPE and the non-causal virtual echo, or VE.

Here the frequency of the electric field is set to 10 GHz and makes the pulse appear dark in the figure. The medium stores the power spectrum of these two pulses, which is shown in (b). The medium's excited state population would be directly proportional to this plot. Notice that there is a periodic spectral structure, that gives rise to the medium's stored spectral grating. The time period of this periodic structure is $1/\tau_{21}$ and the overall spectral width of the grating is related to the temporal width of the individual pulses as $\approx 1/\tau_p$. Finally, (c) shows the output electric field from a probe pulse at t = 30 ns, which was diffracted off of the grating. Notice the echo output at τ_{21} after the probe pulse. One will also notice the non-causal virtual echo, labeled VE, that happens τ_{21} before the probe pulse. The occurrence of this echo is an artifact of the simulation. By causality, only signals which occur after the probe pulse are real.

By using the above framework, the systems response to various types of programming and probing can be predicted. One can use eqn. (2.9), to predict the temporal output from the medium. For example, if the first two input pulses are bandwidth limited temporal delta functions and have temporal widths, τ_1 and τ_2, which are much less than the temporal width, $\delta\tau_3$, of a third input Guassian pulse (pulse widths at FWHM $\tau_1 = \tau_2 \ll \delta\tau_3$), the respective power spectrums of the first two pulses can be considered constant over the bandwidth of the third pulse. Throughout this thesis, if a pulse's total temporal duration is short compared to other pulses incident upon the media, it will be referred to as a brief pulse. Here for example, pulses 1 and 2 are brief pulses. The first two pulses (with $\tau_{21} < T_2$) have a cross term in the

power spectrum with respect to each other giving rise to a periodic spectral feature for $\tilde{H}(\omega)$. The incident third pulse (with $T_2 < \tau_{32} < T_1$) gives the output from the system (the photon echo) whose respective power spectrum is exactly the same as the third Guassian pulse except now with the periodic spectral feature. If the third pulse was centered at a time, t_3 the echo output will occur at $t_3 + \tau_{21}$ due to the periodic spectral feature. This is the description of the SPE process.

Next, assume that the third pulse is not a Guassian pulse, but instead has some temporal structure. Here the fastest temporal structure of the pulse has a width $\delta\tau_3$ and the same condition from above holds ($\tau_1 = \tau_2 \ll \delta\tau_3$). Then, using (2.9), $\tilde{E}_{out}(\omega) \propto \tilde{E}_3(\omega)e^{-i\omega\tau_{21}}$. This means that the SPE will mimic the probe pulse exactly, but delayed by τ_{21}. This is just the TTD process discussed earlier. But echo processes are not limited to just TTD. One may notice that if the first pulse is some arbitrary input starting at t_1 (here the fastest temporal structure is $\delta\tau_1$, the second pulse is a brief reference pulse at t_2 ($\tau_2 << \delta\tau_1$), and the third pulsi is some other arbitrary input pulse starting at t_3 ($\tau_2 << \delta\tau_3$), the echo output is found to be

$$\tilde{E}_{out}(\omega) \approx \tilde{E}_1^{*}(\omega)\tilde{E}_3(\omega)e^{-i\omega\tau_{21}} \ . \tag{2.10}$$

When Fourier transformed to find the time-domain response, this is just the cross-correlation of E_1 and E_3 with a time delay of τ_{21}, which has applications in correlating arbitrary signals with a desired signal [22].

Possible Methods of Solution For The Photon Echo

In the above linear filter theory approach to a solution for the output from the OCT system, several assumptions were made. These were that the input optical pulses were energetically weak, and that the medium was optically thin. If the pulses are energetically weak (i.e. the system is kept from saturating), the system records the power spectrum of the pulse as weak spectral features in the populations. Had the input optical pulses been strong enough to induce saturation, the spectral features stored in the populations are distorted and do not exactly resemble the power spectrum of the pulse that created them. Thus, the predicted output from the system using equation (2.9), would not represent the actual output. Also, the linear filter theory approach (given in eqn. (2.9)) to a solution breaks down as the absorption length increases. There are other approaches to predicting echo phenomena, ranging from easy analytic solutions to computationally complex numerical solutions. This section presents an overview of some possible solution approaches for various situations and their range of validity.

It is important to understand the limitations of the approach being used to predict echo efficiencies in TTD configurations. Figure 5 shows the effect of a thick medium on the power efficiency, η of the 2PE and the SPE for two types of solutions. Here the echo power efficiency, η is defined as the ratio of the echo peak power to the probe pulse peak input power. The probe pulse for the 2PE is the second pulse and the probe pulse for the SPE is the third pulse. In the figure, η is plotted versus the absorption

length (αL) of the medium. In this plot, the pulses were not energetically weak (pulse areas $\Theta_1 = \Theta_2 = \Theta_3 = \pi/2$) and all had the same temporal duration. In the linear regime, η is expected to have a quadratic dependence on αL, as will be discussed later. Quadratic fits predicted from the linear filter theory are shown in this plot with solid lines and labeled with a "Q". This quadratic dependence continues to grow as the thickness of the medium increases, predicting extremely high echo efficiencies for large αL. The numerically integrated solutions, shown with dotted lines and labeled with "MB", were solved with a full Maxwell-Bloch treatment of the medium (discussed below). As can be seen, the Maxwell-Bloch predicted echo efficiency initially follows the quadratic solutions of the linear filter theory. It then begins to fall off, peaking at values of $\alpha L \cong 2$ for the 2PE and $\alpha L \cong 3$ for the SPE. This fall off can be partly attributed to the fact that energy from the incident programming pulses is absorbed by the medium. Thus, further into the medium, the medium sees weaker and weaker programming pulses. At some point, the polarization which produces the echo is no longer creating enough optical energy to compete with the absorption of the medium. Subsequently the echo begins to decay away, as it continues to propagate through the medium. As this plot clearly shows, thick crystals can be utilized to increase echo efficiencies as compared to the optically thin case. However, there is an optimal thickness that depends on the application and programming strengths available.

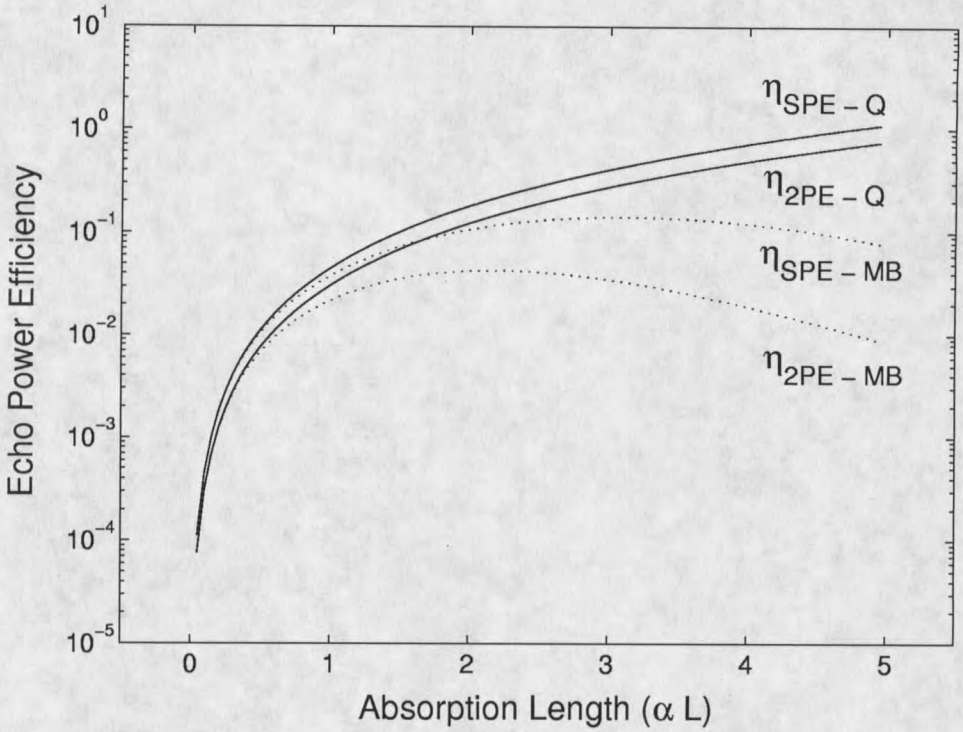

Figure 5. Quadratic fits predicted from linear filter theory (solid and labeled with "Q") and numerical solutions (dashed and labeled with "MB") for the 2PE and the SPE power efficiencies. Here the quadratic solution was valid only for $\alpha L \ll 1$. The numerical solutions were found using a full Maxwell-Bloch treatment of the medium and give a more realistic picture of the true behavior of the system. Here $\Theta_1 = \Theta_2 = \Theta_3 = \pi/2$.

The two solution methods shown in figure 5, represent vastly different amounts of calculational complexity. The linear filter theory, as shown above, results in simple analytic solutions for the output echo. These equations are often very easy to solve but only work under limited conditions. Whereas, the full Maxwell-Bloch treatment for a solution requires direct numerical integration of both the Bloch and Maxwell equations in order to determine the solution but can be used in almost any situation. These computationally intense algorithms can run for hours and require vast amounts

of memory. Solution methods also exist between these two extremes. Over the years many possible methods to predict photon echo processes have been developed [23, 24, 5, 13]. Each of these possible approaches to predicting the outputs are valid under certain conditions. Due to the significant amount of methods, and also the significant amount of conditions for their validity, a "roadmap" is provided here, to help direct the lonely OCT traveler towards a proper predictive tool. In figure 6, this OCT "roadmap" is shown. Here the traveler should start with an input, in this case a specific pulse in a sequence, and proceed to answer the questions on the "road" about that pulse. As a traveler answers questions, he/she will obtain indications about formulas to use, conditions for validity, and ultimately by combining the two, a predictive tool for that specific pulse. This process is repeated for all pulses in a sequence and the resulting formulas and conditions marked down for all the pulses. After all pulses have been processed with the "roadmap", some reflection and thought is required on the part of the traveler. Certain methods can be effectively combined, resulting in quick solutions, which require little computational effort. But sometimes it doesn't pay to mix and match solutions. For instance, if one pulse needs to be completely determined using the full computational complexity of a Maxwell-Bloch simulator, it will make sense to use this simulator for all pulses in the sequence and not worry about trying to combine solutions.

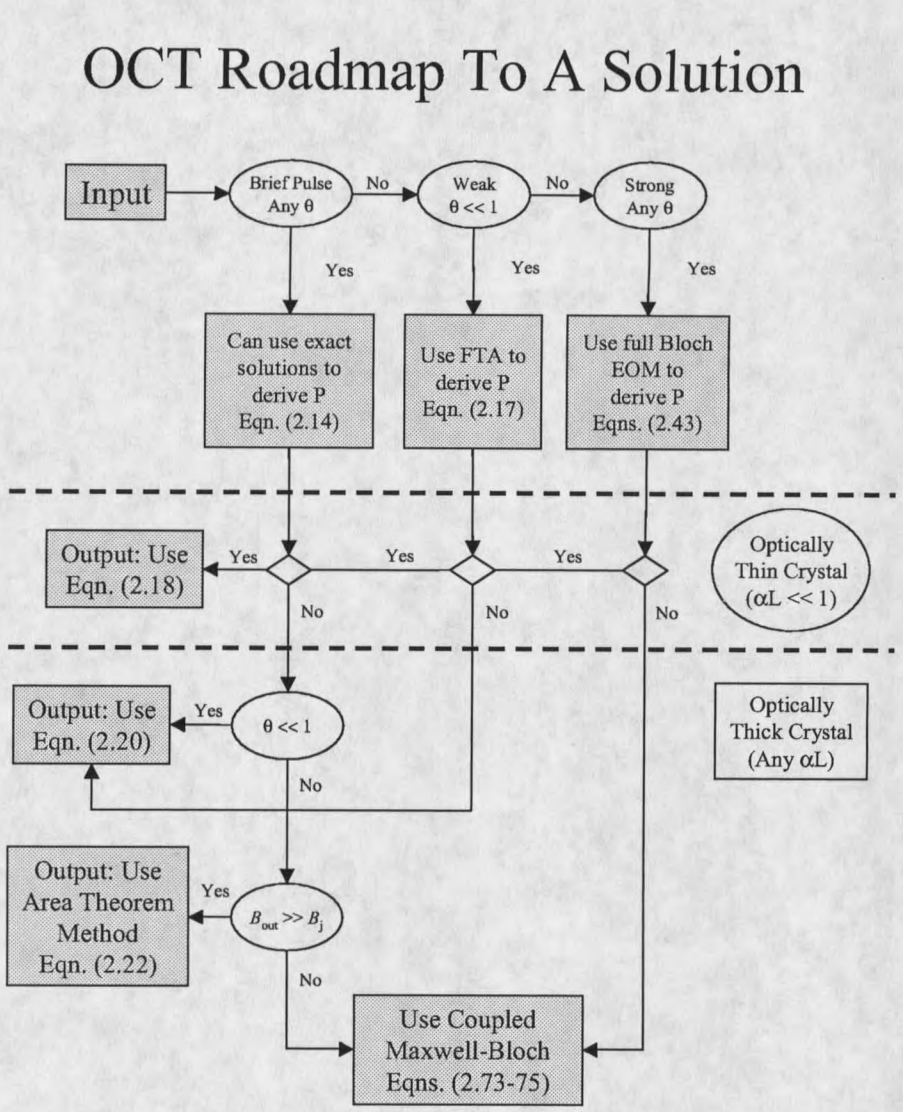

Figure 6. A diagram showing different approaches to a predictive tool for photon echoes. Each pulse in a sequence should be treated with this "roadmap". One asks the specific questions about the pulse, slowly traveling through the "roadmap", marking down the specific conditions, and equations along the way. Once an output is reached an equation for the polarization, P, should have been determined as well as an equation for the output field in terms of that P. Solution types can be mixed, see text for discussion.

The Maxwell wave equation for the OCT medium can be written as

$$\nabla^2 E(z,t) - \frac{n^2}{c^2}\frac{\partial^2}{\partial t^2}E(z,t) = \frac{1}{\varepsilon_o c^2}\frac{\partial^2}{\partial t^2}P(z,t) \ . \tag{2.11}$$

Here $P(z,t)$ represents the macroscopic polarization of the medium. The field is written as

$$E(z,t) = E_o\left(z,t\right)\cos\left(\omega_l t - k_z z + \phi\left(z,t\right)\right) \ . \tag{2.12}$$

Here again, $E_o(z,t)$ is the slowly varying envelope, ω_l is the optical angular frequency, k_z is the wavevector in the direction of propagation and $\phi(z,t)$ is some slowly varying arbitrary phase function. Note that in order to solve for the field, the polarization must be known. However, this polarization is also dependent upon the input field. Thus, there are two major parts for a predictive solution of a photon echo process. The first is to determine the macroscopic polarization within the crystal. This polarization determines the absorption on an input pulse, or subsequently, the emission of light in the form of a photon echo or other free induction decay phenomena. As will be shown later in this chapter, the atomic system for a specific location can be adequately modeled by a set of equations of motion called the Bloch equations. Through the use of these equations, the macroscopic polarization at a specific location in the crystal can be determined for any sequence of pulses. By utilizing certain assumptions, it has been found that these equations can be reduced in complexity. The second part to a solution is to describe the propagation of the field through the medium. When the medium is optically thin, the output electric field from the system is directly

proportional to the macroscopic polarization of the medium. Whereas, in optically thick cases, the optical pulses have to propagate through the medium, and interactions with the medium must be considered at every point along its path. The "roadmap" shown in figure 6 has both of these major components. As a pulse is taken through this "roadmap", equations or approaches to determine the macroscopic polarization, $P(z,t)$ are given as well the proper equations or approaches to predict the propagation effects on the pulses and outputs. Next the approaches to determining the polarization and the propagation are outlined.

Exact Solutions.

Analytic expressions have been derived for a square pulse incident upon a two level system such as the famous solution by I. I. Rabi [25]. This solution, while originally intended for a spin 1/2 system, is applicable to optical pulses incident upon OCT media. If the pulse was a brief pulse, the solution only had a dependence on detuning in the phase factors. A transformation matrix gives a solution for the off diagonal elements of the density matrix as [24]

$$\rho_{12}(t_f) = \rho_{21}^*(t_f) = \cos^2(\Theta_o/2)\,\rho_{12}(t_i) + \sin^2(\Theta_o/2)\,\phi_o^2\rho_{21}^*(t_i) - \frac{i\phi_o}{2}\sin(\Theta_o)\,(\rho_{22}(t_i) - \rho_{11}(t_i)) \ . \tag{2.13}$$

The factor ϕ_o has dependence upon the electric field strength, the dipole moment, and a phase dependence upon the detuning. Here, Θ_o is the pulse area of the incident brief pulse, t_i is the time before the pulse and t_f is the time after application of the pulse.

The macroscopic polarization, for atoms in the inhomogeneously broadened crystal between frequencies ω and $\omega + d\omega$, is dependent upon these off diagonal elements as

$$P(z,t,\omega) = \mu_{12}\rho_{12}(z,t,\omega)\exp(i\omega t)Ng(\omega)d\omega + c.c. \; . \tag{2.14}$$

Here μ_{12} is the dipole moment of the atoms, N is the number density of the atoms, and $g(\omega)$ is a weighting function determined by the inhomogeneous broadening. Through the integration of this equation over ω, the macroscopic polarization can be determined exactly with brief pulses and eqn. (2.13).

Fourier Transform Approximation.

The Fourier transform approximation, originally proposed by T. W. Mossberg [23], utilizes the fact that each frequency component of the optical field acts separately on the resonant atoms of that frequency in the weak field regime. The pulse area, previously defined as Θ is now defined for the frequencies other than the carrier frequency as

$$\Theta(\omega) = \frac{\mu_{12}}{\hbar}\int E_o(t)\,\mathrm{e}^{-i\omega t}\,dt \tag{2.15}$$

If the pulse area for all frequencies is small enough, $\Theta(\omega) \ll 1$ (all ω), the ground state spectral population distribution can be written as

$$\rho_{11}(\omega) \approx 1 - \left(\Theta^2(\omega)/4\right) \; . \tag{2.16}$$

The off diagonal elements are then solved for, using the transformation matrix approach described above. This allows for solution of the macroscopic polarization. The

contribution of this polarization to the SPE for a three pulse sequence can then be solved analytically, giving

$$P(t) = \frac{i|\mu_{12}|^2}{\hbar} \int E_1^*(\omega) E_2(\omega) E_3(\omega)\, \mathrm{e}^{-i\omega(t-\tau_{21})}\, d\omega \ . \tag{2.17}$$

This fundamental result is of tremendous value to the prediction of photon echoes, as was shown above in the linear filter theory. For further discussion of this approach see [24, 5].

Bloch Equations Of Motion.

If the pulses are too strong to treat using the Fourier transform approximation, the full Bloch equations of motion must be utilized. A generalized version of these equations will be derived below, and an expression for the macroscopic polarization, in terms of the Bloch vector components will be given. A numerical solution for this polarization is achievable by following the optical Bloch vector for the set of inhomogeneously broadened atoms. Essentially, the equations of motion for each atom is considered as it is resonant with the frequency components in the optical field.

Thin Crystal $\alpha L \ll 1$.

Along with the approaches to find the polarization, equations to determine the propagation must be considered. Now, the attention is turned to how the polarization, in conjunction with the Maxwell wave equation, can be used to get an output. The easiest approach to solving for the output field from an OCT medium is to assume the

medium is optically thin. As discussed above, this assumption allows the electric field to be directly proportional to the macroscopic polarization, thus, there is no need to take into account the propagation of the output fields. As the medium is optically thin, the absorption of the electric field is negligible and the approach is also known as the undepleted pump approximation. This method allows quick calculations, as no spatial integration is needed, however the regime in which it is valid yields poor echo efficiencies. For a thin αL then, the Fourier transform of the output field is written as [24]

$$E_o(L,\omega) = -\frac{iL\hbar\alpha(\omega)}{2\pi\left|\mu_{12}\right|^2} P(z=0,\omega)\ . \tag{2.18}$$

Here the Fourier transform of the polarization at the front of the medium $P(z = 0,\omega)$ is representative of $P(z,\omega)$ throughout the medium. For the SPE process if $\Theta_1, \Theta_2, \Theta_3, \ll 1$, $P(z=0,\omega)$ is given as

$$P(z=0,\omega) = \frac{i\left|\mu_{12}\right|^2}{\hbar} E_1^*(\omega) E_2(\omega) E_3(\omega)\, \mathrm{e}^{-i\omega\tau_{21}}\ . \tag{2.19}$$

Thick Crystal $\alpha L \gtrsim 1$, Weak Pulses $\Theta \ll 1$.

The propagation effects due to the Maxwell equation, can be utilized in the case for a thick crystal. If $\Theta \ll 1$, the effects of propagation can be adequately handled by Beer's law (2.1), which can be utilized to get an accurate output field. This method allows a simple z dependence of both the output field and the polarization. Essentially, as a field travels into the medium, the field strength will decay exponentially. Thus, the polarization as a function of propagation distance, will decay due to the decay

of the input field. The output field generated also decays due to absorption. The propagation of the field through the medium can then be written [24]

$$\frac{dE_o(z,\omega)}{dz} = -\frac{\alpha(\omega)}{2}E_o(z,\omega) - \frac{iL\hbar\alpha(\omega)}{2\pi\left|\mu_{12}\right|^2}P(z=0,\omega)\exp\left(-\frac{3\alpha(\omega)z}{2}\right) . \quad (2.20)$$

The exponential dependence on z in the term for the polarization is valid for either the 2PE or the SPE process. This equation has been solved exactly as

$$E_o(L,\omega) = -\frac{i\hbar}{2\pi\left|\mu_{12}\right|^2}P(z=0,\omega)\left(1-\exp\left(-\alpha(\omega)L\right)\right)\exp\left(-\frac{\alpha(\omega)L}{2}\right) . \quad (2.21)$$

The polarization is given for the SPE process in eqn. (2.19).

Thick Crystal $\alpha L \gtrsim 1$, Area Theorem Approach.

The approach outlined in eqn. (2.20) requires that the incident optical pulses all be weak. There is another approach to solving for the output in thick media analytically. This approach was outlined by Cornish [13]. In this case, both analytic solutions to the system as well as the Fourier transform approximation were utilized in thick media assuming that $\alpha(\omega)$ is flat over the bandwidth of all incident pulses $\alpha(\omega) = \alpha$. Here, the system responding to a brief pulse can be solved for analytically by utilizing the area theorem. This theorem states that the pulse area must obey [26]

$$\frac{d\Theta(z)}{dz} = -\frac{\alpha}{2}\sin\left(\Theta(z)\right) . \quad (2.22)$$

Through the use of this equation, the overall effect of the pulse on the polarization can be determined at any point in the medium. However, the output pulse shape during the brief pulse can not be determined, only its area. In this case, it is assumed that the

brief pulse need not be energetically weak, but that data pulses are energetically weak. Thus, these data pulses can be solved with the Fourier transform approximation. The systems response to the different pulses is examined after each pulse and then the system is examined where the echo output is expected. In each temporal window, the solution for the pulses are treated with Maxwell's wave equation giving the proper effects due to propagation. Calculations performed in this manner gave analytic echo efficiencies within 1% for brief pulse areas $\Theta_{brief} < 0.6\pi$ of numerically simulated results, as well as adequately predicting the output data shape. Readers are also referred to this method, as it gives a good explanation of how two solution approaches can be used in combination, allowing a combined predictive tool for the output from the medium. As discussed above, brief pulses of any pulse area can be used with this approach. However, due to possible pulse shaping problems [26], the output bandwidth, B_{out}, of the input brief pulse can change. If this output bandwidth is still significantly larger than any other j'th pulse bandwidth, B_j, that is $B_{out} \gg B_j$, it may still be possible to use this approach. However, due to possible pulse reshaping events, such as pulse breakup [19], the signal fidelity predicted using this approach, may be better than that observed in experiments. It is therefor suggested that pulse areas less than π only be used with this approach.

Finally, the system may not be optically thin and the input pulses are all strong, requiring that the Maxwell wave equation be used in conjunction with the optical

Bloch vector. In this situation, the coupled Maxwell-Bloch equations must be directly integrated. These Maxwell-Bloch simulators are very powerful tools as they can handle any arbitrarily shaped pulse, any pulse area, and any optical thickness. However, there are drawbacks. These simulators are computationally demanding and require large amounts of memory. For problems such as accumulated programming sequences, the simulator may need to run for days. Despite these problems, the Maxwell-Bloch simulator has been useful in predicting greater than unit echo efficiencies [12, 10] as well as describing the energy source of the photon echo [13].

Maxwell-Bloch With Arbitrary Phase

Because of the complexity of the equations involved in treating the OCT medium quantum mechanically and including propagation, there are few analytic solutions for an optically thick medium interacting with strong pulses.[1] In order to successfully predict the material's behavior to pulses of arbitrary shape and phase when these pulses are strong and the medium is optically thick one must resort to numerical integration of the Maxwell-Bloch equations.

Bloch simulators, which are based upon numerically integrating the equations of motion for the optical Bloch vector, assume $\alpha L \ll 1$ as discussed above. This was so that the undepleted pump approximation could be assumed and thus the output

[1] See for example the famous self-induced transparency of McCall and Hahn [26]. Another analytic solution utilizing transformation matrices is given in [27] generalizing the McCall and Hahn solution.

electric field would be directly proportional to the macroscopic polarization. In this approximation, all the atoms see the same incident pulses, thus there is no depletion of these pulses as they travel through the medium. These simulators have been successful in predicting the dynamics of the system for many different input pulse sequences including chirped pulses [5]. Issues relating to the timing of echoes, saturation of the media and accumulation of pulse sequences have all been simulated using this approach [5, 28, 29]. However, since the Bloch simulator is limited to optically thin media, the results are not accurate when the output power efficiencies of the echo approach ($\sim 10^{-2}$). As advancements were made in research, it became apparent that the optimal optical thickness is $\alpha L \gtrsim 1$, though the actual optimal value to obtain the highest efficiency varies with application. However, the highest efficiency is not always the best [30] due to the effects of saturation. Along with efficiency, the fidelity of the echoes must be examined and ultimately, a balance between efficiency and good fidelity sought. In order to predict and study these phenomena, simulators based upon the coupled Maxwell-Bloch equations were developed. These simulators were used to predict highly efficient photon echo generation [12, 10] before their detection [11] for an optical storage application. The utility of such simulators, allows the dynamics of the population gratings and coherences to be followed through the thick medium. With these tools, the energy source for the photon echo was also determined [13].

The goal of this thesis is to demonstrate TTD of a broad bandwidth signal, with high efficiencies and good signal fidelity. It is known that chirped programming

provides a better overall method to achieve OCT TTD. To date, however, Maxwell-Bloch simulators have been based upon a field whose arbitrary phase function is zero. If the electric field is written

$$E(z,t) = E_o(z,t)\cos(\omega_l t - k_z z + \phi(z,t)) \ , \tag{2.23}$$

the previous simulators kept $\phi = 0$. Note that $E_o(z,t)$ is the time dependent, slowly varying envelope function, which allows arbitrarily shaped pulses. The requirement that $\phi = 0$ does not allow simulation of pulses that have frequency shifts with respect to each other or for frequency chirped pulses. Thus, to properly study echo efficiencies, signal fidelity, and echo timing, the full Maxwell-Bloch equations, including arbitrarily ramping phase, had to be used. A simulator based upon these equations can then be utilized to study the power efficiencies, signal fidelities, and timing of gratings programmed with frequency offset linear frequency chirps. Ultimately, this simulator can be used to predict the optimal absorption length for efficient, high fidelity echoes. It is through this optimization and subsequent improvement in echo strength that will make OCT TTD applications attractive.

Two Level Systems and the Bloch Equations

In order to begin a discussion on the Maxwell-Bloch equations, one must have a bit of background in the quantum mechanical treatment of two level systems and their interaction with electric fields. The two levels in the system are described as $|1\rangle$ and $|2\rangle$ for the ground state and excited state, respectively. If the energy difference

between the two levels is $\hbar\omega_a$, the Hamiltonian, $\hat{H}_o$, for the time independent two level system is then

$$\hat{H}_o = \begin{pmatrix} 0 & 0 \\ 0 & \hbar\omega_a \end{pmatrix} . \tag{2.24}$$

If an electric field, such as in eqn. (2.23) is introduced the Hamiltonian must be modified. The generalized Hamiltonian, $\hat{H}$, can be found by adding a term to the time independent Hamiltonian that appropriately takes into account the interaction of the system with the electric field. Thus $\hat{H}$ can be written

$$\hat{H} = \hat{H}_o + \hat{V}(z,t) . \tag{2.25}$$

This interaction, $\hat{V}(z,t)$ is described by the dipole interaction

$$\hat{V}(z,t) = -\hat{\mu}E(z,t) = -\begin{pmatrix} 0 & \mu_{12} \\ \mu_{21} & 0 \end{pmatrix} E(z,t) . \tag{2.26}$$

It is assumed that the field, $E(z,t)$ and the dipole moment are aligned and that dipole moment operator acts between the levels of interest. In this case, we do not consider transitions between levels of different spin, and therefore do not account for changes in polarizations of the fields. With these assumptions, $\mu_{12} = \mu_{21} = \mu$ and can be assumed real for simplicity. Finally, the total Hamiltonian can be expressed as

$$\hat{H} = \begin{pmatrix} 0 & -\mu E(z,t) \\ -\mu E(z,t) & \hbar\omega_a \end{pmatrix} . \tag{2.27}$$

In order to obtain the Bloch equations, the density matrix formalism will be used. For the two level system, the density matrix elements are

$$\hat{\rho} = \begin{pmatrix} \rho_{11} & \rho_{12} \\ \rho_{21} & \rho_{22} \end{pmatrix} . \tag{2.28}$$

The equation of motion, or Schroedinger's equation, using a density matrix is given by

$$\begin{aligned} \dot{\rho} &= \frac{i}{\hbar}[\rho, H] \\ &= \frac{i}{\hbar}(\rho H - H\rho) \end{aligned} \tag{2.29}$$

The differential equations for the individual density matrix elements are then

$$\begin{aligned} \dot{\rho_{11}} &= \frac{i\mu E(z,t)}{\hbar}(\rho_{21} - \rho_{12}) \\ \dot{\rho_{12}} &= \frac{i}{\hbar}(\mu E(z,t)(\rho_{22} - \rho_{11}) + \hbar\omega_a \rho_{12}) \\ \dot{\rho_{21}} &= \left(\dot{\rho_{12}}\right)^* \\ \dot{\rho_{22}} &= -\dot{\rho_{11}} \,. \end{aligned} \tag{2.30}$$

To simplify the equations, it is common to choose a rotating frame. This rotating frame allows terms that are rapidly varying (frequencies of order $2\omega_a$) compared to the timescale of interest to be dropped. To do this the frame is rotated at a constant angular frequency, ω_o, which is close to the transition frequency. Now the density matrix elements, $\hat{\varrho}_{ij}$ in the rotating frame are defined as

$$\begin{aligned} \varrho_{11} &= \rho_{11} \\ \varrho_{22} &= \rho_{22} \\ \varrho_{12} &= \rho_{12} e^{-i\omega_o t} \\ \varrho_{21} &= \rho_{21} e^{i\omega_o t} \,. \end{aligned} \tag{2.31}$$

Taking the eqns. (2.30) and substituting in the rotating frame elements gives the on-axis elements

$$\begin{aligned} \dot{\varrho}_{11} &= \frac{i\mu E(z,t)}{\hbar}\left(\varrho_{21}e^{-i\omega_o t} - \varrho_{12}e^{i\omega_o t}\right) \\ \dot{\varrho}_{22} &= -\dot{\varrho}_{11}\ . \end{aligned} \tag{2.32}$$

Using the off-axis description in eqn. (2.30) and taking the time derivative of eqn. (2.31) gives the off-axis equation

$$\dot{\varrho}_{12} = \dot{\rho}_{12}e^{-i\omega_o t} - i\omega_o\rho_{12}e^{-i\omega_o t}\ . \tag{2.33}$$

Substituting in from eqn. (2.30) gives

$$\begin{aligned} \dot{\varrho}_{12} &= \left(\frac{i}{\hbar}\left(\mu E(z,t)\left(\varrho_{22}-\varrho_{11}\right) + \hbar\omega_a\varrho_{12}e^{i\omega_o t}\right)\right)e^{-i\omega_o t} - i\omega_o\varrho_{12} \\ &= \frac{i}{\hbar}\mu E(z,t)\left(\varrho_{22}-\varrho_{11}\right)e^{-i\omega_o t} + i\left(\omega_a-\omega_o\right)\varrho_{12} \\ \dot{\varrho}_{21} &= \left(\dot{\varrho}_{12}\right)^* \end{aligned} \tag{2.34}$$

Now the electric field can be entered and the formulas simplified. Here the electric field is rewritten as follows

$$E(z,t) = \frac{\hbar}{2\mu}\Omega(z,t)\left(e^{i(\omega_l t - k_z z + \phi(z,t))} + e^{-i(\omega_l t - k_z z + \phi(z,t))}\right)\ . \tag{2.35}$$

Notice that the envelope function has been changed to have frequency units, $\Omega(z,t) = \frac{\mu}{\hbar}E_o(z,t)$, where an explicit z and t dependence of the field is assumed. Entering the

electric field into the eqn. (2.32) the on-axis elements become

$$\begin{aligned}\dot{\varrho}_{11} &= \frac{i\mu}{\hbar}\left(\varrho_{21}e^{-i\omega_o t} - \varrho_{12}e^{i\omega_o t}\right)\frac{\hbar}{2\mu}\Omega\left(e^{i(\omega_l t - k_z z + \phi(z,t))} + e^{-i(\omega_l t - k_z z + \phi(z,t))}\right) \\ &= \frac{i\Omega}{2}\left(\varrho_{21}e^{-i\omega_o t}e^{i(\omega_l t - k_z z + \phi(z,t))} + \varrho_{21}e^{-i\omega_o t}e^{-i(\omega_l t - k_z z + \phi(z,t))}\right. \\ &\quad \left. -\varrho_{12}e^{i\omega_o t}e^{i(\omega_l t - k_z z + \phi(z,t))} - \varrho_{12}e^{i\omega_o t}e^{-i(\omega_l t - k_z z + \phi(z,t))}\right)\end{aligned}$$

Notice that there are two terms in this last equation that oscillate extremely rapidly, one with $e^{i(\omega_o+\omega_l)t}$ and its complex conjugate. This oscillation essentially averages to zero on the time scale of the change in the density matrix elements and the two terms can be dropped or neglected. This is known as the rotating wave approximation. In this case then, the expression becomes

$$\dot{\varrho}_{11} = \frac{i\Omega}{2}\left(\varrho_{21}e^{i((\omega_l-\omega_o)t - k_z z + \phi(z,t))} - \varrho_{12}e^{-i((\omega_l-\omega_o)t - k_z z + \phi(z,t))}\right) . \tag{2.36}$$

By defining $\gamma = (\omega_l - \omega_o)t - k_z z + \phi(z,t)$ the equations further simplify to

$$\begin{aligned}\dot{\varrho}_{11} &= \frac{i\Omega}{2}\left(\varrho_{21}e^{i\gamma} - \varrho_{12}e^{-i\gamma}\right) \\ &= \frac{\Omega}{2}\left(i(\varrho_{21} - \varrho_{12})\cos\gamma - (\varrho_{21} + \varrho_{12})\sin\gamma\right) .\end{aligned} \tag{2.37}$$

And the off axis elements become

$$\dot{\varrho}_{12} = i\left(\omega_a - \omega_o\right)\varrho_{12} + \frac{i}{2}\Omega e^{i\gamma}\left(\varrho_{22} - \varrho_{11}\right) , \tag{2.38}$$

after the rotating wave approximation is made. Finally, the elements of the Bloch

vector in the rotating frame, $\vec{r}$, are defined as

$$\begin{aligned} r_1 &= \varrho_{21} + \varrho_{12} \\ r_2 &= i(\varrho_{21} - \varrho_{12}) \\ r_3 &= \varrho_{22} - \varrho_{11} \ . \end{aligned} \tag{2.39}$$

The time derivative for r_1 is

$$\begin{aligned} \dot{r_1} &= \dot{\varrho_{21}} + \dot{\varrho_{12}} \\ &= -i\left(\omega_a - \omega_o\right)\varrho_{21} - \frac{i}{2}\Omega e^{-i\gamma}\left(\varrho_{22} - \varrho_{11}\right) + i\left(\omega_a - \omega_o\right)\varrho_{12} + \frac{i}{2}\Omega e^{i\gamma}\left(\varrho_{22} - \varrho_{11}\right) \\ &= -i(\varrho_{21} - \varrho_{12})\left(\omega_a - \omega_o\right) + \frac{i}{2}\Omega\left(\varrho_{22} - \varrho_{11}\right)\left(e^{i\gamma} - e^{-i\gamma}\right) \\ &= -\left(\omega_a - \omega_o\right)r_2 - \Omega r_3 \sin\gamma \ . \end{aligned} \tag{2.40}$$

Similarly r_2 is found to be

$$\begin{aligned} \dot{r_2} &= i\left(\dot{\varrho_{21}} - \dot{\varrho_{12}}\right) \\ &= i\left(-i\left(\omega_a - \omega_o\right)\varrho_{21} - \frac{i}{2}\Omega e^{-i\gamma}\left(\varrho_{22} - \varrho_{11}\right) - i\left(\omega_a - \omega_o\right)\varrho_{12} - \frac{i}{2}\Omega e^{i\gamma}\left(\varrho_{22} - \varrho_{11}\right)\right) \\ &= \left(\omega_a - \omega_o\right)\left(\varrho_{21} + \varrho_{12}\right) + \frac{i}{2}\Omega\left(\varrho_{22} - \varrho_{11}\right)\left(e^{-i\gamma} + e^{i\gamma}\right) \\ &= \left(\omega_a - \omega_o\right)r_1 + \Omega r_3 \cos\gamma \ . \end{aligned} \tag{2.41}$$

And finally for r_3,

$$\begin{aligned} \dot{r_3} &= \dot{\varrho_{22}} - \dot{\varrho_{11}} = -2\dot{\varrho_{11}} \\ &= -2\left(\frac{\Omega}{2}\left(i(\varrho_{21} - \varrho_{12})\cos\gamma - (\varrho_{21} + \varrho_{12})\sin\gamma\right)\right) \\ &= \Omega r_1 \sin\gamma - \Omega r_2 \cos\gamma \ . \end{aligned} \tag{2.42}$$

These equations give the time evolution of the Bloch vector, otherwise known as the Bloch equations and can be used to effectively determine the localized effect of the field on the medium.

$$\begin{aligned} \dot{r_1} &= -(\omega_a - \omega_o)\, r_2 - \Omega r_3 \sin\gamma \\ \dot{r_2} &= (\omega_a - \omega_o)\, r_1 + \Omega r_3 \cos\gamma \\ \dot{r_3} &= \Omega r_1 \sin\gamma - \Omega r_2 \cos\gamma \end{aligned} \tag{2.43}$$

Maxwell-Bloch Derivation

If the field, defined in eqn. (2.23), acts upon the medium and in turn the medium acts back on the field, then the classical Maxwell equations must be coupled with the Bloch equations in order to predict the output from the medium. Note that through eqn. (2.35) solutions are restricted to forward propagating fields. Here, the Maxwell equation can be written in the rest frame as

$$\nabla^2 E(z,t) - \frac{n^2}{c^2}\frac{\partial^2}{\partial t^2}E(z,t) = \frac{1}{\varepsilon_o c^2}\frac{\partial^2}{\partial t^2}P(z,t) \tag{2.44}$$

Here the envelope of the field, the phase (and thus the Bloch vectors) are assumed to be slowly varying with respect to the optical frequency. This assumption, known as the slowly varying envelope approximation, will be used below to drop small terms [31]. Using the field as defined in eqn. 2.23, the slowly varying envelope approximation assumes

$$\frac{\partial E_o}{\partial z} \ll k_z E_o \;,\; \frac{\partial E_o}{\partial t} \ll \omega_l E_o \;,\; \frac{\partial \phi}{\partial z} \ll k_z \;,\; \frac{\partial \phi}{\partial t} \ll \omega_l \;,\; \frac{\partial r_i}{\partial t} \ll \omega_l r_i \;. \tag{2.45}$$

To determine the effect of the medium on the field, the macroscopic polarization must be determined. The macroscopic polarization is given by a weighted integral over all the atoms in the medium. The inhomogeneous broadening is assumed to be a Guassian function given by

$$g(\omega_a) = g_o \exp\left(-\left(\frac{\omega_a - \omega_c}{\sigma_i}\right)^2\right) . \tag{2.46}$$

Here ω_c is the center frequency of the inhomogeneous line, σ_i is the half width at the $1/e$ point of the inhomogeneous line, and g_o is the normalization, which has units of time. Here the normalization can be calculated as

$$\frac{1}{2\pi}\int_0^\infty g(\omega)d\omega = 1 . \tag{2.47}$$

The macroscopic polarization, $P(z,t)$, written in the rest frame is defined as

$$P(z,t) = \frac{N\mu}{2\pi}\int_0^\infty [r_1 \cos(\omega_o t - k_z z) - r_2 \sin(\omega_o t - k_z z)]g(\omega)d\omega . \tag{2.48}$$

By taking the second derivative with respect to time for (2.48) and dropping terms that are small given by (2.45) one finds

$$\frac{\partial^2}{\partial t^2}P(z,t) \cong \frac{N\mu\omega_l^2}{2\pi}\int [r_2 \sin(\omega_o t - k_z z) - r_1 \cos(\omega_o t - k_z z)]g(\omega)d\omega . \tag{2.49}$$

Now, the attention is turned to the left hand side of eqn. (2.44). Again using the approximations in (2.45), the second derivative of the field with respect to z can be expressed as

$$\nabla^2 E(z,t) \cong E_o\left(-{k_z}^2 + 2k_z\frac{\partial\phi}{\partial z}\right)\cos(\omega_l t - k_z z + \phi) + 2k_z\frac{\partial E_o}{\partial z}\sin(\omega_l t - k_z z + \phi) . \tag{2.50}$$

Likewise, the second derivative of the field with respect to time can be found as

$$\frac{\partial^2}{\partial t^2}E(z,t) \cong E_o\left(-\omega_l^2 - 2\omega_l\frac{\partial\phi}{\partial t}\right)\cos\left(\omega_l t - k_z z + \phi\right) - 2\omega_l\frac{\partial E_o}{\partial t}\sin\left(\omega_l t - k_z z + \phi\right) \ . \tag{2.51}$$

By combining the last two equations with the left hand side of eqn. (2.44) and by using the relation $k_z = n\omega_l/c$ gives

$$\begin{aligned}\nabla^2 E(z,t) - \frac{n^2}{c^2}\frac{\partial^2}{\partial t^2}E(z,t) = {} & 2E_o\left(k_z\frac{\partial\phi}{\partial z} + \frac{n^2\omega_l}{c^2}\frac{\partial\phi}{\partial t}\right)\cos\left(\omega_l t - k_z z + \phi\right) \\ & +2\left(k_z\frac{\partial E_o}{\partial z} + \frac{n^2\omega_l}{c^2}\frac{\partial E_o}{\partial t}\right)\sin\left(\omega_l t - k_z z + \phi\right) \ .\end{aligned} \tag{2.52}$$

Now the two sides of eqn. (2.44) can be equated. This gives

$$\begin{aligned} & 2E_o\left(k_z\frac{\partial\phi}{\partial z} + \frac{n^2\omega_l}{c^2}\frac{\partial\phi}{\partial t}\right)\cos\left(\omega_l t - k_z z + \phi\right) \\ + \ & 2\left(k_z\frac{\partial E_o}{\partial z} + \frac{n^2\omega_l}{c^2}\frac{\partial E_o}{\partial t}\right)\sin\left(\omega_l t - k_z z + \phi\right) \\ = \ & \frac{N\mu\omega_l^2}{2\pi\varepsilon_o c^2}\int\left[r_2\sin\left(\omega_o t - k_z z\right) - r_1\cos\left(\omega_o t - k_z z\right)\right]g(\omega)d\omega \ . \end{aligned} \tag{2.53}$$

Up to here, the rotating frame has been generalized to rotate at a frequency, ω_o, that is close to the atomic frequency, ω_a. This was done so that any of the common rotating frames could be chosen, such as the laser frame or atomic frame. However, here it becomes necessary that the laser frame be chosen ($\omega_o = \omega_l$). The goal at this point is to try to equate like cosines and sines in order to get two equations, one for $\phi(z,t)$ and one for $E_o(z,t)$. But it is noticed that the terms on the right hand side of eqn. (2.53) are missing terms for the $\phi(z,t)$. This requires that some trigonometric

equations be used namely,

$$\cos(a+b) = \cos a \cos b - \sin a \sin b$$

$$\sin(a+b) = \sin a \cos b + \cos a \sin b \; . \tag{2.54}$$

Here $a = \omega_l - k_z z$ and $b = \phi(z,t)$. With this relation, one finds the expression

$$\begin{aligned} & A\{\cos a \cos b - \sin a \sin b\} \\ + \; & B\{\sin a \cos b + \cos a \sin b\} \\ = \; & C \int [r_2 \sin a - r_1 \cos a] g(\omega) d\omega \; , \end{aligned} \tag{2.55}$$

with

$$\begin{aligned} A &= 2E_o \left(k_z \frac{\partial \phi}{\partial z} + \frac{n^2 \omega_l}{c^2} \frac{\partial \phi}{\partial t} \right) \\ B &= 2 \left(k_z \frac{\partial E_o}{\partial z} + \frac{n^2 \omega_l}{c^2} \frac{\partial E_o}{\partial t} \right) \\ C &= \frac{N \mu \omega_l^2}{2\pi \epsilon_o c^2} \; . \end{aligned} \tag{2.56}$$

Now the like sines and cosines can be equated on both sides giving two equations

$$B \cos b - A \sin b = C \int r_2 g(\omega) d\omega \tag{2.57}$$

$$A \cos b + B \sin b = -C \int r_1 g(\omega) d\omega \; . \tag{2.58}$$

These expressions can be rewritten after a little trigonometry and algebra as

$$B = C \int \{r_2 \cos b - r_1 \sin b\} \, g(\omega) d\omega \tag{2.59}$$

$$A = -C \int \{r_1 \cos b + r_2 \sin b\} \, g(\omega) d\omega \; . \tag{2.60}$$

Inserting the coefficients given by (2.56) one finds two equations, one for the slowly varying field amplitude and one for the slowly varying phase

$$\left(\frac{\partial\phi}{\partial z}+\frac{n\omega_l}{c}\frac{\partial\phi}{\partial t}\right)=-\frac{N\mu\omega_l}{4\pi E_o\varepsilon_o nc}\int\{r_1\cos\phi+r_2\sin\phi\}g(\omega)d\omega \tag{2.61}$$

$$\left(\frac{\partial E_o}{\partial z}+\frac{n\omega_l}{c}\frac{\partial E_o}{\partial t}\right)=\frac{N\mu\omega_l}{4\pi\varepsilon_o nc}\int\{r_2\cos\phi-r_1\sin\phi\}g(\omega)d\omega\ . \tag{2.62}$$

Finally, by switching to a frame that moves at the speed of light in the medium [32] in the +z direction, one can essentially eliminate derivatives with respect to time. This is done as follows. Allow a new coordinate, t', in a new frame such that

$$t'=t-\frac{n}{c}z\ ,\ \frac{\partial t}{\partial t'}=1\ ,\ \frac{\partial t'}{\partial z}=-\frac{n}{c}+\frac{\partial t}{\partial z}\ . \tag{2.63}$$

With some math the phase and field can now be written in the new frame as

$$\frac{\partial\phi'(z,t')}{\partial z}=-\frac{1}{E_o'}\frac{N\mu\omega_l}{4\pi\varepsilon_o nc}\int[r_1\cos(\phi')+r_2\sin(\phi')]g(\omega)d\omega \tag{2.64}$$

$$\frac{\partial E_o'(z,t')}{\partial z}=\frac{N\mu\omega_l}{4\pi\varepsilon_o nc}\int[r_2\cos(\phi')-r_1\sin(\phi')]g(\omega)d\omega \tag{2.65}$$

Note that the phase and the amplitude functions have been redefined in the new frame as E_o' and ϕ', and are equivalent to the old functions when $z=0$. Notice that the equations have been reduced to two coupled first order differential equations with respect to the propagation coordinate, z. This allows numerical integration assuming there is only propagation in the forward direction (positive z). Finally, the absorption coefficient, α, written in terms of the material parameters is

$$\alpha=\frac{N\mu^2\omega_c g_o}{2\varepsilon_o\hbar nc}\ . \tag{2.66}$$

Next it is assumed that the laser is operating at the center of the inhomogeneous transition ($\omega_l = \omega_c$) given by eqn. (2.46). Also, a substitution from ω to detuning, $\Delta = \omega_a - \omega_o$ has been performed. Thus, the limits of the integration are now switched from 0 to ∞ to $-\infty$ to ∞, assuming that the weighting function is small for large Δ. The eqns. (2.64) and (2.65) are then rewritten to include the absorption coefficient, detuning, and Rabi frequency as

$$\frac{\partial \phi'(z,t')}{\partial z} = -\frac{1}{\Omega'}\frac{\alpha}{2\pi}\int (r_1 \cos(\phi') + r_2 \sin(\phi'))\exp\left(-(\Delta/\sigma_i)^2\right)d\Delta \qquad (2.67)$$

$$\frac{\partial \Omega'(z,t')}{\partial z} = \frac{\alpha}{2\pi}\int (r_2 \cos(\phi') - r_1 \sin(\phi'))\exp\left(-(\Delta/\sigma_i)^2\right)d\Delta \ . \qquad (2.68)$$

Finally, two equations relating the slowly varying phase and amplitude to the first two elements of the Bloch vector have been obtained. With the above definitions for detuning and because of the moving frame, $\gamma = \phi'(z,t')$ and the Bloch equations can be written

$$\dot{r_1} = -\Delta r_2 - \Omega r_3 \sin\phi \qquad (2.69)$$

$$\dot{r_2} = \Delta r_1 + \Omega r_3 \cos\phi \qquad (2.70)$$

$$\dot{r_3} = \Omega r_1 \sin\phi - \Omega r_2 \cos\phi \qquad (2.71)$$

As these equations were to be numerically integrated, the above equation for ϕ' (2.67) has the difficulty of being inversely proportional to Ω'. This can introduce numerical complexities that can be easily avoided by keeping track of the in-phase

and in-quadrature parts of the field. By defining

$$\Omega_c(z,t') = \Omega'(z,t')\cos(\phi')$$
$$\Omega_s(z,t') = \Omega'(z,t')\sin(\phi')\ , \tag{2.72}$$

the Bloch equations simplify to

$$\begin{aligned} \dot{r_1} &= -\Delta r_2 - \Omega_s r_3 \\ \dot{r_2} &= \Delta r_1 + \Omega_c r_2 \\ \dot{r_3} &= \Omega_s r_1 - \Omega_c r_2 \end{aligned} \tag{2.73}$$

and the propagation equations then become

$$\frac{\partial \Omega_c}{\partial z} = \frac{\alpha}{2\pi}\int r_2 \exp\left(-(\Delta/\sigma_i)^2\right)d\Delta \tag{2.74}$$
$$\frac{\partial \Omega_s}{\partial z} = -\frac{\alpha}{2\pi}\int r_1 \exp\left(-(\Delta/\sigma_i)^2\right)d\Delta\ . \tag{2.75}$$

These equations are numerically integrated to give the Bloch vector $\vec{r}(z,t',\Delta)$ for all z, time and detunings. The field components $\Omega_c(z,t')$ and $\Omega_s(z,t')$ are also found for all z and time. Finally, the square of the field, $|\Omega'(z,t')|^2$, is proportional to the observed intensity, and can be found from

$$|\Omega'(z,t')|^2 = \Omega_c(z,t')^2 + \Omega_s(z,t')^2\ . \tag{2.76}$$

The phase can be calculated from

$$\phi'(z,t') = \arctan\left(\frac{\Omega_s(z,t')}{\Omega_c(z,t')}\right). \tag{2.77}$$

Maxwell-Bloch Simulations

Throughout this thesis, the above Maxwell-Bloch equations are numerically integrated in a specially developed Maxwell-Bloch simulator. The simulator has a graphical front end, which allows the user easy access to the simulators parameters and a pictorial view of the input sequence of pulses. The graphical user interface was created using Visual C++ and is designed to run on a 32-bit Windows platform. A screen shot of the graphical front end is shown in figure 7. The output from this front end is a start file that contains all the information needed to run a simulation. The actual numerical integrator, the heart of the simulator, is itself a separate program and takes the start file as input. The separation was done for practical purposes. In this fashion, the numerical integrator can be fully optimized and easily compiled without having to deal with the graphical front end. The numerical integration code is also platform independent C++ code that can be compiled and run on many operating systems, UNIX©, LYNIX, or Windows©. This allows time consuming, parallel computations to be run on the campus supercomputer, Bigdog. Also, many versions of numerical integrators can be used for the same start file. Along with these benefits, the graphical front end can control the starting of the numerical integrator on separate computers. It transfers the start file and begins the numerical integration. It also handles the output from the numerical integrator and can display various outputs using the graphical package contained within a popular program called MATLAB®. All of these features allow easy, quick simulations to be performed.

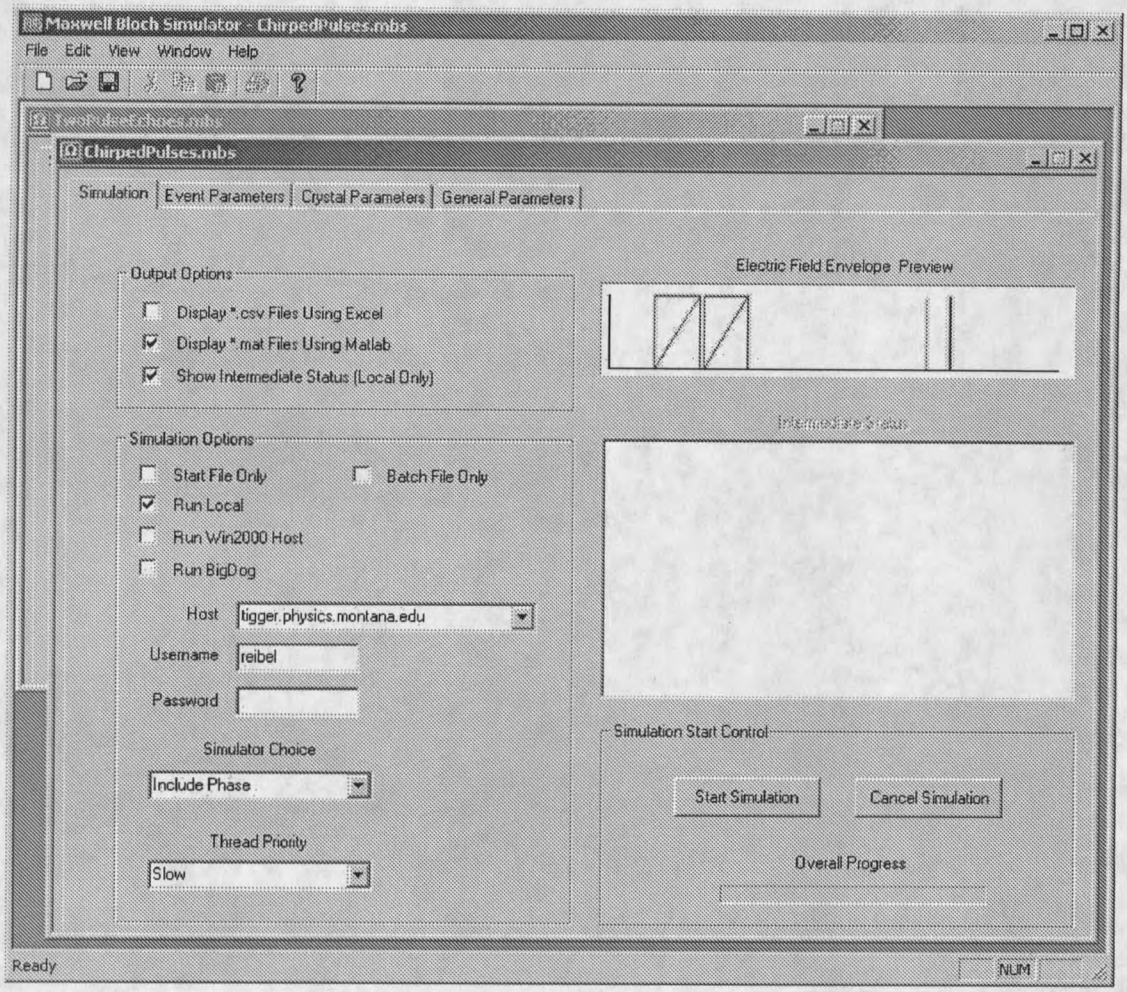

Figure 7. A screen shot of the Maxwell-Bloch simulator's graphical user interface used to enter parameters and start simulations.

As an example and a check of the simulators abilities, some different sequences are shown here but many are also included in the subsequent chapters. First, a simulation of the experimental echo sequence shown in figure 3 is given. Here the pulses are of Guassian envelope with FWHM's of 100 ns, $\tau_{21} = 1100$ ns, each pulse area at zero detuning was $\pi/2$ and $\alpha L = 1.4$. This sequence was simulated and the output is

shown in figure (8). The input sequence (dotted line) is shown as well as the outputs, including the expected echoes (solid line). The echoes are observed at the proper time delay with efficiencies of $\sim 5\%$ for the 2PE and $\sim 10\%$ for the SPE. The pulse area for the 2PE has been calculated using the proper analytic solutions [13] and agrees to within $\sim 3\%$ of the simulated 5% efficiency result.

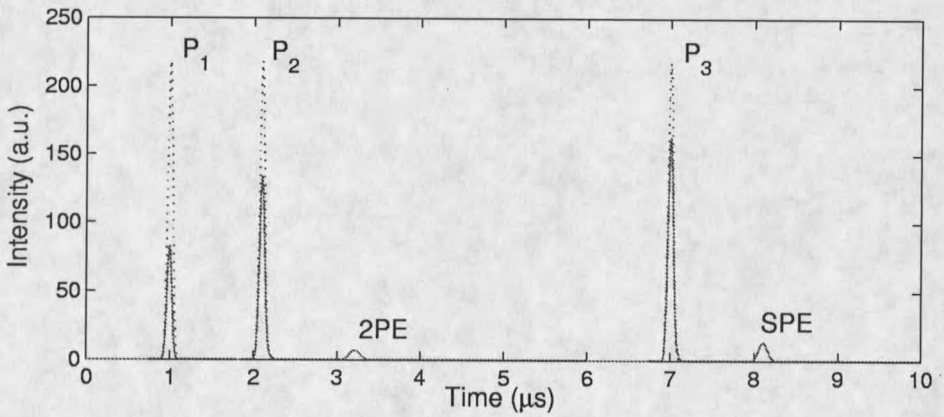

Figure 8. A simulated echo sequence showing the 2PE and the SPE for an $\alpha L = 1.4$.

This suggests that the simulator is predicting the output appropriately. Further checks are shown later in this chapter. One of the nice aspects of numerical simulators is that they allow easy analysis of the medium's properties at any time. In other words, the individual components of the Bloch vector can be analyzed at any time and for different locations within the medium. This can be very helpful in analyzing the response of the medium's populations and coherences to a complicated series of pulses. For example, the spectral grating can be seen in the parameter, r_3. The

grating, shown in the top of figure 9, is a snapshot at time 5 μs at an $\alpha L \approx 0.3$. The value of r_3 is shown for all frequency detunings that were simulated. While this dependence could have been analyzed with a simple Bloch simulator, the Maxwell-Bloch simulator allows the detuning to be examined at any αL, whereas the Bloch simulator is limited to $\alpha L \ll 1$. An example grating from the same sequence is also shown in the bottom of figure 9, this time for an $\alpha L = 1.4$.

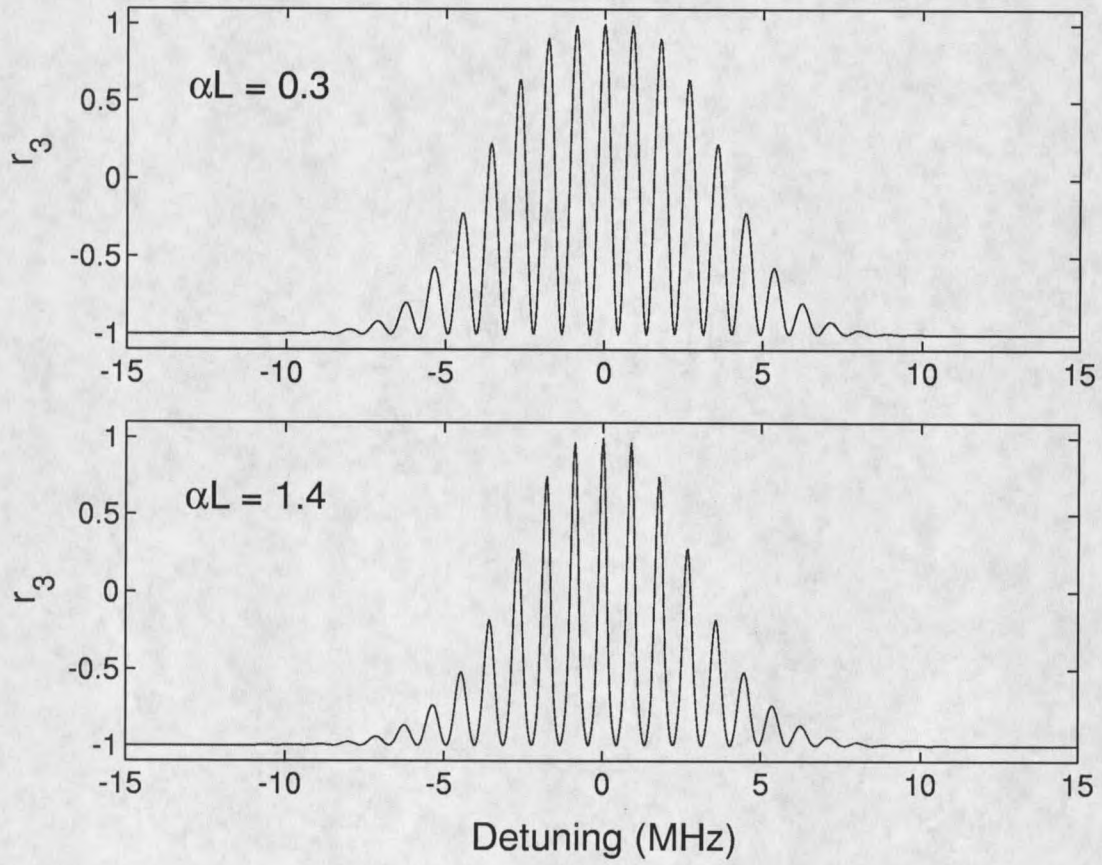

Figure 9. The population grating, stored in the r_3 component of the Bloch vector versus detuning at time 5 μs from the above echo sequence. The top plot shows the grating for an $\alpha L \approx .3$, and the bottom plot shows the grating for an $\alpha L \approx .3$.

Along with being able to analyze the components of the Bloch vector for any point within the crystal and at various times, the output field and phase are also known. Thus, the propagation of the input pulses and their corresponding absorption can be analyzed. The echo can also be analyzed and a picture of how the echo's amplitude grows as a function of propagation is also investigated. These effects are shown in figure 10 for the 2PE and in figure 11 for the SPE.

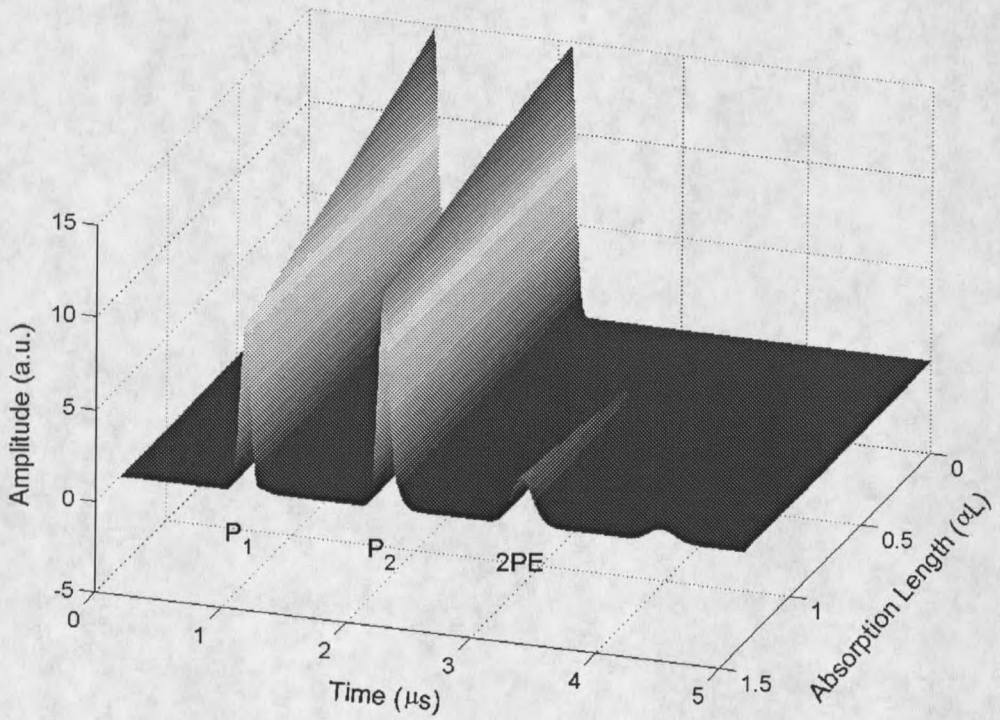

Figure 10. The field amplitude for various times and absorption length of the first two pulses and the 2PE.

The medium starts in the ground state, and picks up energy from the initial pulses traveling into the medium. This can be seen as an overall absorption on the input

pulses as they propagate through the medium. As can be seen from figures 10 and 11, the echo typically starts with a very small amplitude for small αL, and as it propagates through the medium, picks up energy and grows in amplitude. It was verified that this energy is essentially transferred from the populations, r_3, at the time of the echo leading to the mechanism for the energy source of the photon echo [13].

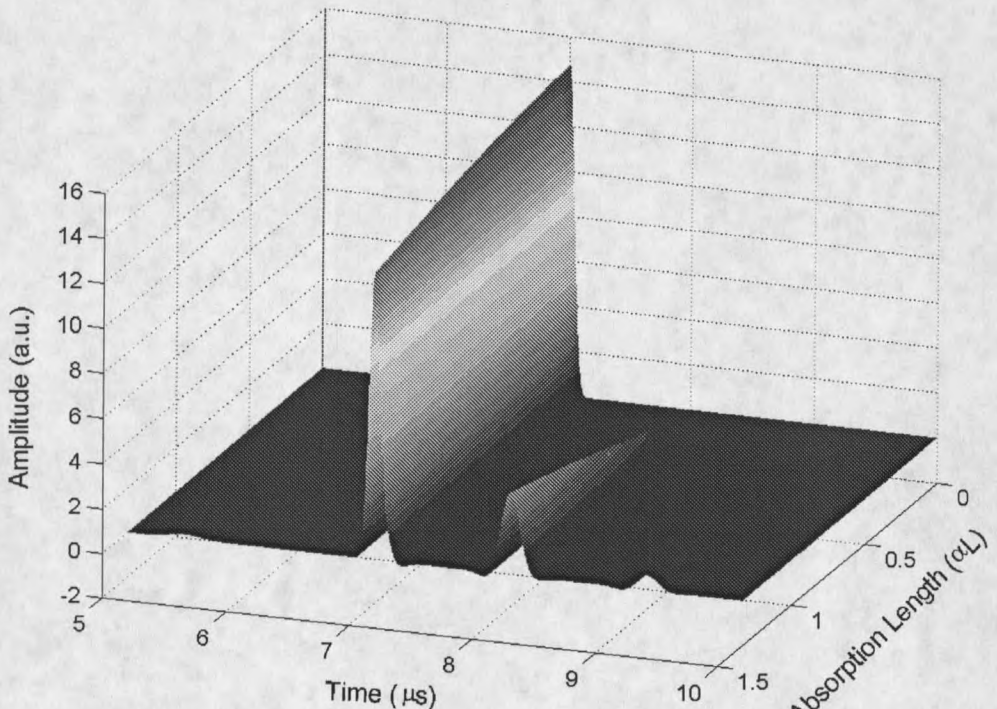

Figure 11. The field amplitude for various times and absorption length of the probe pulse and the SPE.

A further check to see if the simulator was behaving properly was to analyze sequences in the optically thin regime. In this regime both the intensities of the 2PE and the SPE should show quadratic dependence on the absorption length. The echo

power efficiencies, η, are expected to follow

$$\eta_{2PE} = \sin^4(\Theta_2/2)(\alpha L)^2 \tag{2.78}$$

$$\eta_{SPE} = \frac{1}{4}\sin^2(\Theta_2)\sin^2(\Theta_3)(\alpha L)^2 \tag{2.79}$$

for a weak first pulse and $\alpha \ll 1$ [24]. Here the efficiency is with respect to the first pulse, which is considered the data pulse as described above ($\tau_1 \gg \tau_2 = \tau_3$). In the simulations above, the pulse area on resonance of each pulse was $\pi/2$ and they all had the same bandwidths, thus violating these conditions for power efficiency. Thus eqns. (2.78) and (2.79) do not apply for this case, except as an upper bound on the efficiency. The actual efficiency is worse than when the conditions do apply. This is essentially because the second and third pulse do not act as $\pi/2$ pulses over the whole bandwidth of the first pulse. The power efficiency was confirmed to obey eqns. (2.78) and (2.79) by running another simulation for thin media. In this simulation, $\tau_1 \gg \tau_2 = \tau_3$, and the pulse areas were $\Theta_1 = 0.01\pi$, $\Theta_2 = 0.5\pi$, and $\Theta_3 = 0.5\pi$, thus the conditions for the validity of the power efficiency held. In this situation, eqn. (2.78) and (2.79) give $\eta = 1/4(\alpha L)^2$ for both the 2PE and the SPE. This was observed as shown in figure 12. Here the simulated power efficiencies for 2PE (o's) and SPE (x's) are shown versus absorption length. The solid line is (2.78) and (2.79). The exact match in the linear regime shows that the simulator is behaving appropriately.

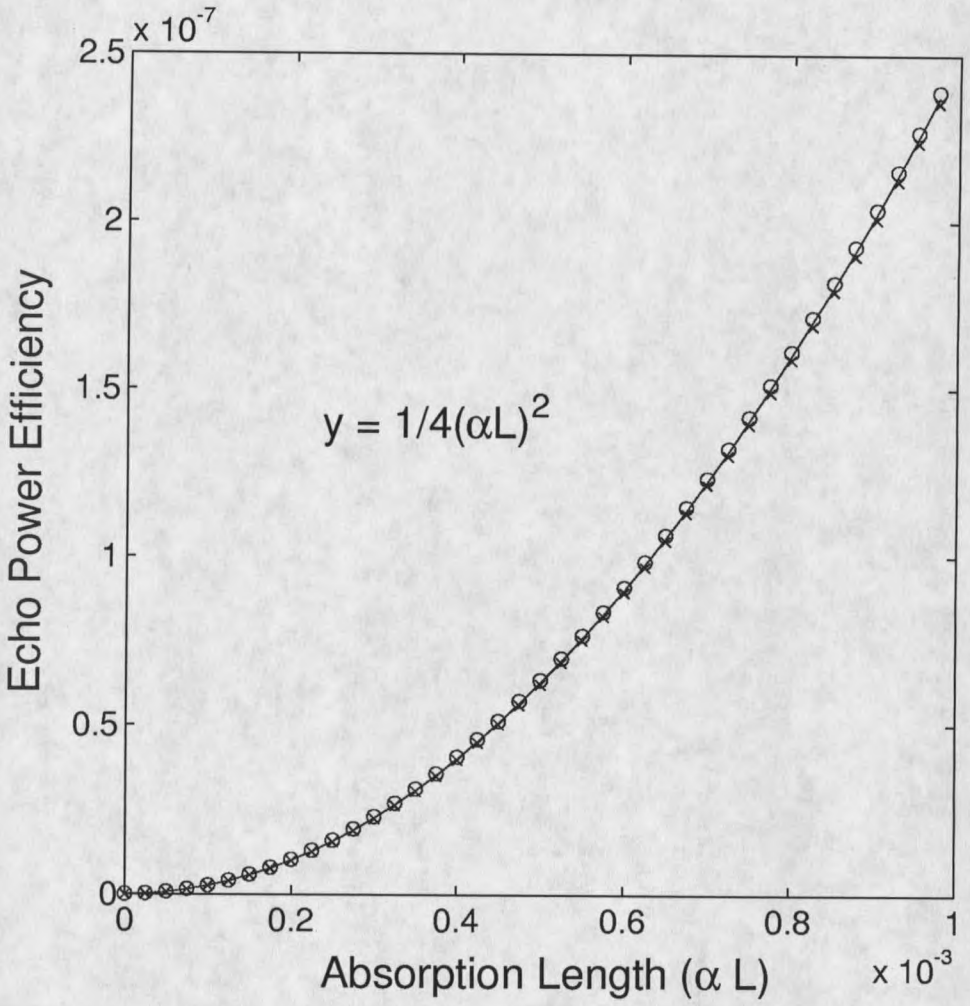

Figure 12. The simulated power efficiencies for 2PE (o's) and SPE (x's) are shown versus absorption length. The solid line is the quadratic analytic solution with a coefficient of 1/4. Here $\tau_1 \gg \tau_2 = \tau_3$, and the pulse areas were $\Theta_1 = 0.01\pi$, $\Theta_2 = 0.5\pi$, and $\Theta_3 = 0.5\pi$.

The above echo sequences used $\phi' = 0$. However, the newly developed simulator has the necessary equations to properly handle arbitrary phase functions. One very important type of pulse, the linear frequency chirp, can be simulated by using the phase envelope function

$$\phi' = \pi\gamma(t - t_s)^2 \ . \tag{2.80}$$

Here $\gamma = B/\tau_C$ is defined as the chirp rate of the pulse with B as the bandwidth and τ_C as the chirp duration. It is typical to allow this chirp to be centered around ω_l, however the simulator allows one to choose the offset. Note that the phase is synchronized with the front of the chirped pulse at time, t_s. In figure (13) two 1 μs chirped pulses are incident upon the medium ($\alpha L = 1.4$) separated by $\tau_{21} = 1.1$ μs. These two pulses, behave similarly to two brief pulses and program a time delay grating over the bandwidth that they chirp (40 MHz in this case). Here the Ω's of each chirp were set to 1.7 MHz. The probe pulse, P_3, is then incident upon this grating and creates an SPE that comes with the appropriate delay of 1.1 μs.

The spectral grating for linear frequency chirped programming has a flatter profile than its brief pulse counterpart as seen in figure 14. The spectral grating has a period that is the inverse of the programmed delay and can be used to create a stimulated photon echo.

Linear frequency chirps have several advantages for programming TTD gratings. One advantage is that, as can be seen in figure 13, the echo is more efficient with this type of programming method. Here the echo efficiency is $\sim 20\%$, which is twice as

large as the equivalent brief pulse programming scheme shown in figure 8. Chapter 3 includes a discussion of this effect, including simulations of power efficiencies for optically thick crystals. Then later, in chapter 5, other advantages of linear frequency chirped programming will be discussed.

Any phase function, assuming it is slowly varying compared to the optical frequency, can be numerically integrated using this Maxwell-Bloch simulator. This allows pulses with frequency shifts, CW phase modulated pulses, binary phase shift keyed (BPSK) pulses, amplitude and phase modulated pulses, along with many others to be simulated and studied. In each of these cases, one must remember that in order for the approximations given by (2.45) to hold, slowly varying functions of the phase must be represented. The phase can not be discontinuous but must be ramped continuously for each of these types of arbitrary types of phase modulated pulses. All of these types of pulses have been tested in the simulator, and some are presented in the appropriate sections with experimental data.

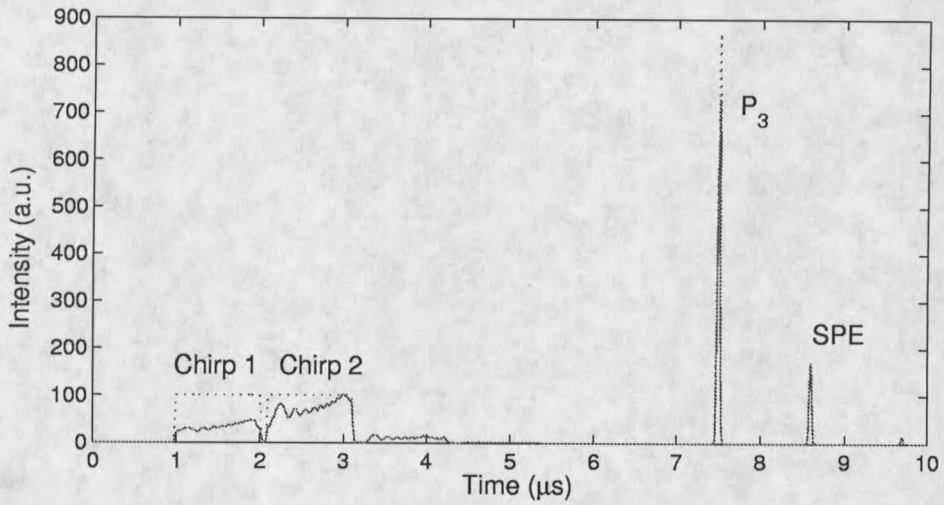

Figure 13. The input and output intensities for a chirped pulse sequence from a crystal with $\alpha L = 1.4$. Here the echo efficiency is $\sim 20\%$.

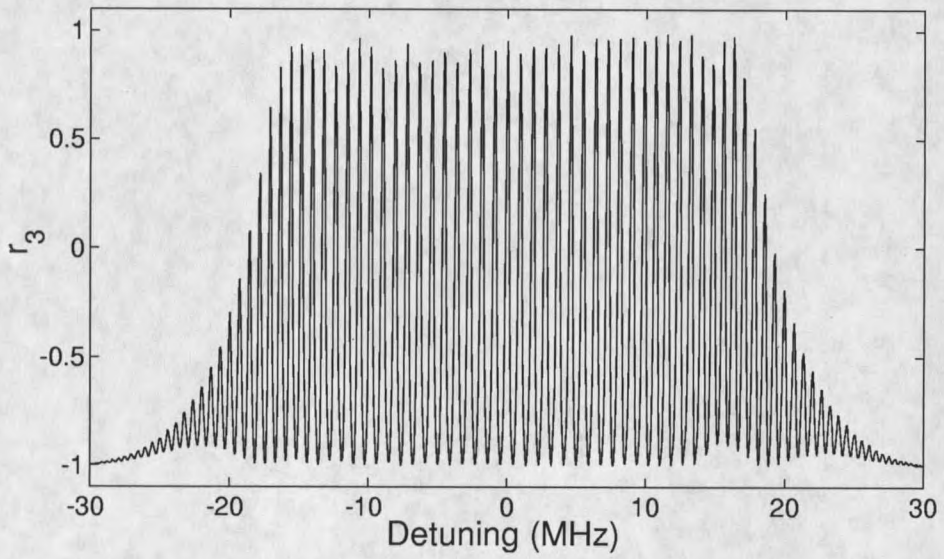

Figure 14. The r_3 component of the Bloch vector as a function of the detuning. This shows the spectral grating created by two linear frequency chirped pulses. Here $\alpha L = 1.4$ and $t = 5$ μs.

CHAPTER 3

PRACTICAL CONSIDERATIONS FOR HIGH BANDWIDTH OCT PROGRAMMING

In order to achieve high bandwidth OCT TTD, several practical issues must be sorted out. There are considerations with the material, OCT programming and probing, as well as high bandwidth modulation and detection. For example, the materials TBP's must be considered as well as lifetimes, as they play a crucial role in determining on what time scale and over what bandwidths TTD can be achieved. Along with this, the material parameters play a role in efficient programming and probing of OCT's. Since efficient spectral gratings are desired, the issues of how to program them into the OCT medium must be discussed. Other programming schemes have resulted in better than unit echo efficiencies [11, 12, 10]. These efforts were interested in data storage, and not in TTD. Thus the power efficiencies for TTD must be considered for desired programming methods using optically thick media. Another important issue, is that even if an efficient high bandwidth spectral grating is programmed, one must understand the limitations or nonlinear effects that can be expected when probing this spectral grating. These limitations have been studied before [30], and there relevance to the probing schemes for TTD should be examined. Finally, if these probes are to be high bandwidth signals, such as BPSK signals, the implications of how to create and detect these probes must be understood. For

large bandwidth probe signals the effects due to the inhomogeneous broadening may become important. Also, can the spectral grating be utilized to filter broadband signals in an efficient way creating better methods for detection of these signals?

This chapter discusses all of these important practical considerations to achieving high bandwidth OCT TTD. In the first section, the material parameters for Tm^{3+}:YAG will be presented. In the second section, a discussion of the implications for programming efficient TTD gratings is examined. This is followed by a brief overview of possible problems in probing these gratings. Finally, how to create and detect phase modulated signals is the topic of the last section. This last section concludes with a treatment on how the bandwidth of the crystal may influence these phase modulated signals as well as how spectral gratings can act as highly efficient filters for detecting phase modulated signals.

Material Considerations

There are many possible materials that could be used for spatial-spectral holography (SSH). Some possibilities were presented in chapter 2, and include rare-earth ion doped crystals, gasses of heated atoms, and systems of large organic molecules. Each of these materials has benefits and possible applications in various situations. It turns out, however, that for practical uses such as OCT TTD or other processes such as correlation or memory storage, rare-earth ion doped crystals have several strong advantages. These advantages include compactness, large TBP's, transitions

at popular laser lines (~790 nm, ~1530 nm), long T_2's and T_1's, and low cost. [33]

Because of these advantages, the experiments performed in this thesis use the $^3H_6$ - $^3H_4$ transition in 0.1% atomic Tm^{3+}:YAG. A representation of the atomic levels is shown in figure 15. This transition's resonant frequency is 793 nm. The overall defect and spectral properties of this crystal were studied by Wang and can be found in reference [17]. Spectral hole burning on the trivalent thulium ion was first observed by Macfarlane [34] as well as the first photon-echo measurements [14]. This crystal has a bottleneck state, the $^3F_4$ level. The electrons in the $^3H_4$ level decay either to the $^3H_6$ or the $^3F_4$ with a branching ratio, β, of approximately 0.56 and a decay time, T_1, of $\sim$ 600 μs.[1] The electrons on the $^3F_4$ level also decay to the $^3H_6$ level with a lifetime, T_3, of $\sim$ 12 ms [36]. Dephasing times have been reported as $\sim$ 20 μs and can range depending upon experimental conditions from a few μs to more than 30 μs as will be discussed in the following chapters. The inhomogeneous broadening's FWHM is approximately 20 GHz. For the longer T_2's, the TBP is roughly 10^6 for this crystal. These material parameters are highly suited for broadband TTD. Expected delays of several microseconds on broadband (>20 GHz) signals can be expected. Thus Tm^{3+}:YAG is a good candidate material for a TTD system.

1

The $^3H_5$ level has an energy between the $^3H_4$ and the $^3F_4$ levels but the lifetime of this level, estimated to be 0.1-1.0 μs [35], is insignificant compared to the bottleneck lifetime and can thus be ignored.

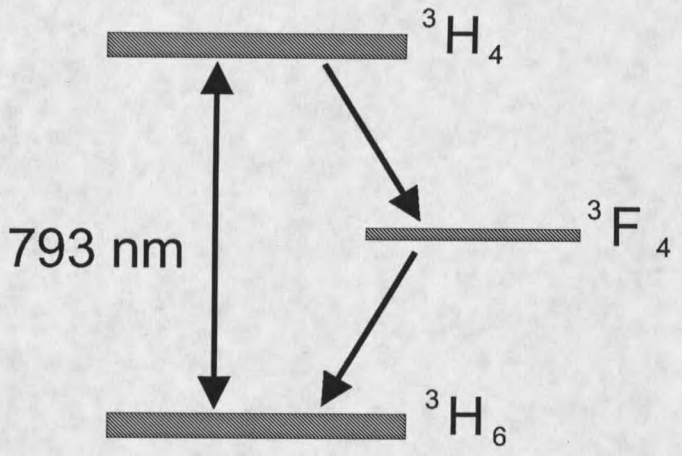

Figure 15. The atomic levels of interest for this thesis for the rare-earth ion doped crystal Tm^{3+}:YAG.

OCT Programming Efficiencies and Considerations

As was stated in the introduction to this chapter, there are several important considerations when programming or probing a spectral grating in an OCT medium. As programming spectral gratings is pushed to higher bandwidths, perhaps the most important consideration is the efficiency of the programmed grating. The efficiency of a grating, η, is defined as the ratio of the peak echo intensity, I_e, to the peak intensity of the probe, I_p. That is

$$\eta = \frac{I_e}{I_p} \,. \tag{3.1}$$

Echo efficiencies for single shot, low bandwidth experiments are usually 1-3% for $\alpha L \approx 1$. However, as higher bandwidths are reached, the optical pulse has to excite more and more atoms, spread out over a larger bandwidth. This means that in order

to keep the efficiency the same, the probe must transfer more optical energy into the medium. For brief pulses, the only way to do this is to increase the power of the brief pulse, since the brief pulses temporal duration must get shorter to program a wider bandwidth. In order to reach multi-gigahertz bandwidths, picosecond pulses must be used.

In our lab, these pulses can be created from a mode-locked Ti:Sapphire laser, and along with a regenerative amplifier, can produce very powerful pulses, $\sim 10^9$ Watts. However, even with these large powers, it is still difficult to program an efficient spectral grating. The reason for this is that the pulses can not be focused too tightly into the crystal, or crystal surface damage will result. At a conservative spot size within the crystal of ~ 200 μm, grating efficiencies are extremely low. For a single shot experiment, efficiencies of $\sim 10^{-5}$ are expected for brief pulse programming with a pulse area of 0.05 π. Compared with low bandwidth single shot experiments, this efficiency is clearly very low.

There are three main programming approaches that can help to improve grating efficiencies. The first is to use programming pulses that can spread their bandwidths over time, such as linear frequency chirps. This alleviates the problems associated with brief pulse programming because the temporal duration of the pulse can now be longer, while still programming large bandwidths. The second approach is to use optically thicker crystals. The third approach is to repetitively apply the programming pulses. Ideally, this should enhance the spectral grating and allow build up of

a stronger, more efficient grating. Of course all of these techniques could be used in combination, further enhancing the grating efficiency.

Grating Efficiency vs. Bandwidth

As was discussed in chapter 2, LFC pulses are a more efficient solution for programming compared to using brief pulses. However, achieving maximum efficiency requires optimizing the chirp parameters. The efficiency of a grating, η, was defined above in eqn. (3.1). This efficiency is equivalent to what is also termed the power efficiency, used by other authors [13]. First, the efficiency of chirps is compared to the brief programming pulse method. Then the power efficiency of these two methods is simulated and compared for optically thick crystals.

It can be shown that if a spectral grating was programmed by a series of brief programming pulses, the echo efficiency would fall as approximately $1/B^4$ if the peak intensity of the pulse is fixed. [2] In the linear regime, the echo signal in the frequency domain, $E_e(\omega)$ can be found from the relation [37]

$$E_e(\omega) \propto E_1^*(\omega) E_2(\omega) E_p(\omega) \ . \tag{3.3}$$

Here $E_1(\omega)$ and $E_2(\omega)$ are the Fourier transforms of the first and second pulses of

[2] This can easily be seen as the energy in a power limited brief pulse will drop as the temporal duration, τ_p, is shortened. The energy drops by $\tau_p^2 = 1/B^2$. Since the energy in the time domain is equivalent to the energy in the spectral domain, the power efficiency can be written as

$$\eta = \left| \frac{E_e(\omega)}{E_p(\omega)} \right|^2 = |E_1^*(\omega)|^2 |E_2(\omega)|^2 \propto 1/B^4 \ . \tag{3.2}$$

Thus the power efficiency for brief pulse programming very rapidly decreases as a function of bandwidth for power limited lasers.

the programming sequence respectively and $E_p(\omega)$ is the Fourier transformed probe pulse. If the frequency chirps have a field amplitude in the time domain of E_c and $E_1^*(\omega)E_2(\omega)$ is assumed flat over B and zero outside of B, that is $|E_1(\omega)| = |E_2(\omega)| = E_o$ on the interval $2\pi B$ of the LFC, then it can be shown, using Parseval's theorem, that the following relation holds

$$E_o = E_C\sqrt{\frac{\tau_C}{B}}\,. \tag{3.4}$$

Using this equation, and $I \propto \langle E^2 \rangle$ by definition, the intensity of the echo is found to be

$$I_e \propto E_C^4 \left(\frac{\tau_C}{B}\right)^2 I_p\,. \tag{3.5}$$

And using eqn. (3.1) the efficiency in the linear regime can be written as

$$\eta \propto E_C^4 \left(\frac{\tau_C}{B}\right)^2\,. \tag{3.6}$$

This equation shows that the echo efficiency with chirped pulse programming is proportional to $1/B^2$, and thus chirps offer an immediate advantage over brief pulses. This is basically because as a chirp's bandwidth is increased, its temporal duration can stay constant. Whereas for brief pulses, the duration must decrease in order to program a larger bandwidth. LFC programming has the added benefit of having the echo intensity proportional to τ_C^2. Thus, the longer the chirp duration, the stronger the echo will be in the linear regime. So if the bandwidth is increased, the drop in efficiency can be compensated for by increasing the chirp time to keep the chirp rate

constant. This can be done provided that the chirps are completed within the bottleneck lifetime of the medium. It is these traits that make LFC pulse programming an attractive, practical solution for high bandwidth TTD.

The functional dependence of eqn. (3.6) was examined using the Maxwell-Bloch simulator for media that are not optically thin, in this case $\alpha L = 1.4$. This was done for two different situations. The first situation, kept τ_C constant while varying B. A series of 100 simulations were done with programming B's from 20 MHz to 60 MHz in steps of 0.4 MHz. The probe pulse had a bandwidth of 10 MHz. The equivalent Rabi frequency, Ω_{eq}, for a chirped pulse acting with a $\pi/2$ pulse area for a 4 μs, 20 MHz chirp is calculated as $\sim$0.6 MHz using the formula [22][3]

$$\Omega_{eq} = 0.27\sqrt{\frac{B}{\tau_C}} \,. \tag{3.7}$$

This simulation had a Rabi frequency of $\Omega = 0.125$ MHz, keeping it below the $\Omega_{eq} =$ 0.42 MHz for the lowest bandwidth of 20 MHz. Here the time delay was controlled using frequency offsets, δ's, which will be discussed in chapter 5. These frequency offsets were varied to keep the time delay constant at 0.8 μs. In figure 16, the circles are the simulated echo efficiencies versus the programming bandwidth. As can be seen, the echo intensity decreases as a function of the bandwidth as expected. The $1/B^2$ analytic solution is also plotted as the solid line. The dashed line is representative of the brief pulse programming method dropping off as $1/B^4$. One can see

[3] The author independently verified that this equivalent Rabi frequency gives an $r_3(\Delta = 0) = 0$ and an average $r_3(\omega)$=0 over the bandwidth of the chirp to within $\pm$3% for various bandwidths and chirp durations.

a slight deviation in the simulation output as compared to the analytic solution in the optically thin regime. Overall, the efficiency does not appear to be significantly affected by the absorption length, $\alpha L = 1.4$.

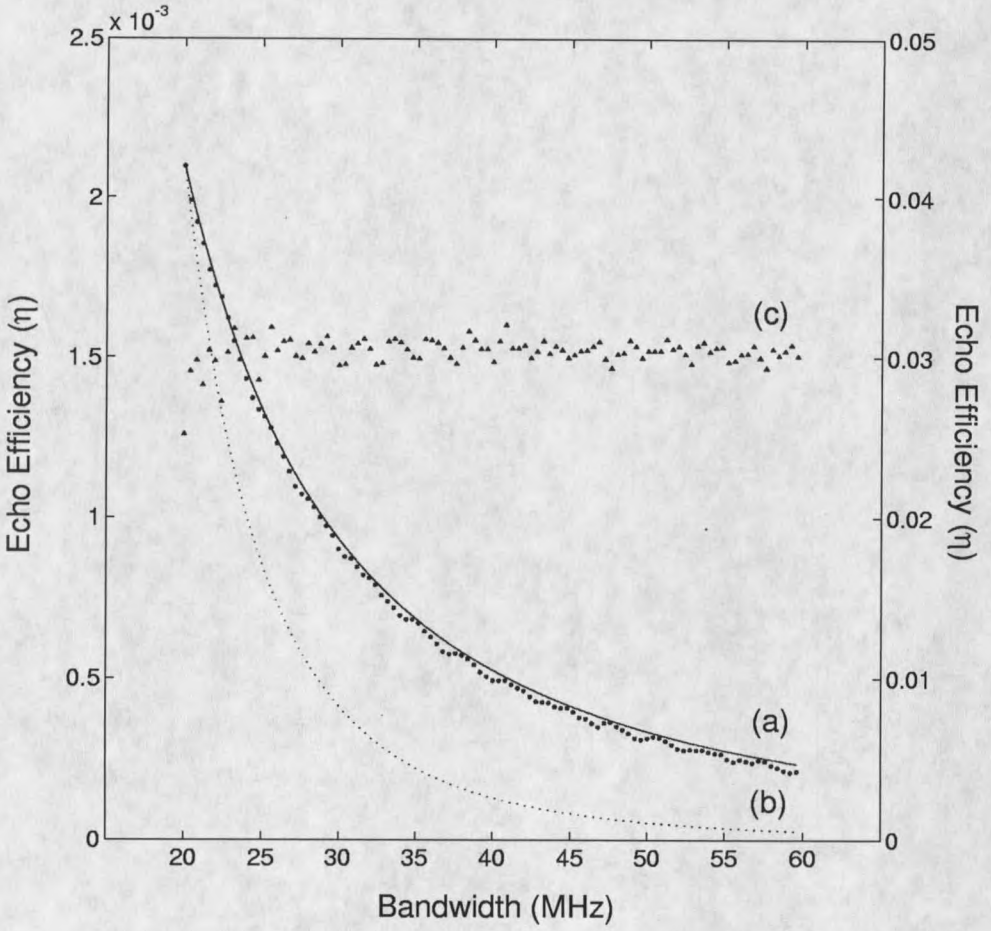

Figure 16. Data points showing simulated peak echo height versus bandwidth for constant programming powers. Here $\tau_C = 4$ μs and δ is varied to keep τ_D constant. The solid line is calculated using the analytic functional dependence of $1/B^2$ (normalized). The dashed line is a plot of the analytic dependence of a brief pulse programming versus bandwidth and is normalized to the first point in the $1/B^2$ sequence for contrast. The triangles are simulated sequences for a constant τ_C/B ratio with efficiencies given by the right hand axis.

The second situation is when the ratio τ_C/B is kept constant. In this case, there should be roughly no change in echo efficiency. This situation is plotted as the triangles in figure 16. Here the righthand vertical axis gives the echo efficiencies for this plot. As can be seen, the simulated echo efficiencies for this situation remain relatively constant. This set of simulations was done with B's from 20 MHz to 60 MHz in steps of 0.4 MHz. Here the τ_C's ran from 2 μs to 6 μs in steps of 0.04 μs, and $\delta = 8$ MHz giving a constant $\tau_D = 0.8$ μs. Ω's here were 0.5 MHz over the whole simulation. Note that the calculated ratio in efficiency (using eqn. (3.6) between the constant sequence and the $B = 20$ MHz point of the $1/B^2$ sequence is a factor of 16. The simulated value using an average of $\eta = 0.03$ for the constant sequence gives a ratio of 13.7. The slight decrease from the expected value is most likely due to the fact that the constant sequence is further from the linear regime with an $\Omega = 0.5$ MHz. Here the calculated equivalent Rabi frequency is $\Omega_{eq} = 0.84$ MHz. The small fluctuations can be attributed to the fact that the bandwidth of the probe pulse and the time delays are of the same order as will be discussed in a later chapter. This situation shows the advantage of using LFC pulses for programming with a power limited laser. Here, as the bandwidth is increased, the efficiency of the grating can be kept constant if more optical energy is transferred to the medium by increasing the chirp duration. Ultimately, it is by balancing the τ_C/B ratio that high bandwidth gratings can be programmed efficiently into the OCT medium.

Highly Efficient TTD Using Chirped Programming

As was discussed briefly at the end of chapter 2, linear frequency chirped programming is a more efficient programming method. This could be seen in figure 13 where the echo was 2 times as efficient compared to the similar brief pulse programming case shown in figure 8. In this section, echo power efficiencies are examined as a function of the pulse areas (or Rabi frequencies) of the programming, as well as a function of αL for TTD programming.

Figure 17 shows the various input sequences studied in this section. In (a) a data storage programming scheme is shown. This programming scheme was extensively studied by C. Cornish [13] and was the first programming scheme where greater than unit power efficiencies were predicted [12] and observed [11]. This scheme is studied here as a check on the new Maxwell-Bloch simulator for large αL.

Here, the first pulse in the sequence is a brief pulse with a significant pulse area, Θ_1. The second pulse in the sequence is known as a data pulse, and has a bandwidth less than the first pulse and also has low pulse areas, Θ_2. Finally, at a later time, the stored data can be recalled by a probe pulse identical to the first pulse with a significant pulse area, Θ_p, stimulating an echo representative of the data pulse.

This sequence was simulated using the Maxwell-Bloch simulator, with the same parameters found in the work done by C. Cornish [13]. The power efficiency is plotted as a function of αL for various $\Theta_1 = \Theta_P = A$, ranging from 0.1 π to 0.7 π in figure 18.

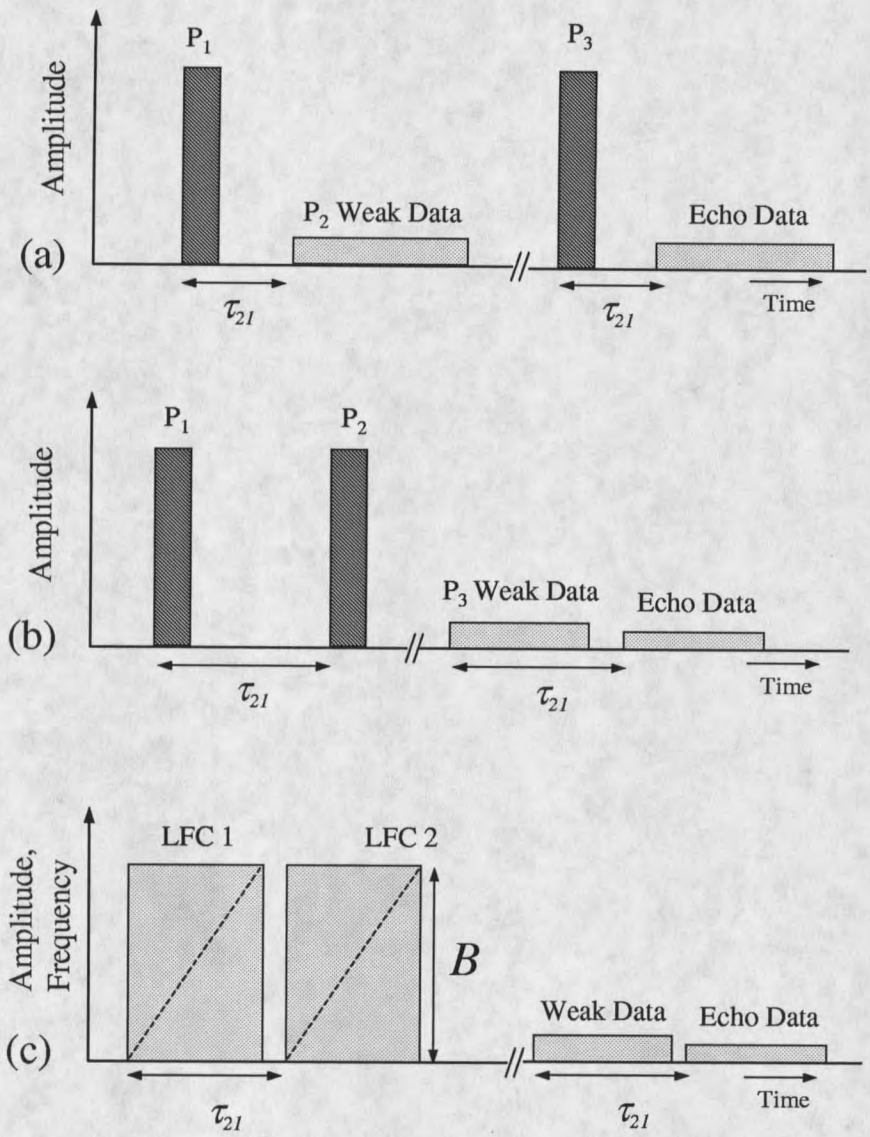

Figure 17. Illustrations of each of the simulated input sequences studied for this thesis. In (a) a data storage configuration is shown. This configuration has shown better than unit efficiencies (see text) and is simulated here for comparison with new arbitrary phase Maxwell-Bloch simulator. (b) A brief programming pulse scheme for programming TTD echo sequences. (c) A linear frequency chirped programming scheme for producing TTD echo sequences.

Here the first and third pulses were Guassian with FWHM's of 0.1 ns. The data pulse was also Guassian and had a FWHM of 0.4 ns and $\Theta_2 = 0.01\pi$. As can be seen in the plot, efficiencies greater than unity are predicted around $\alpha L = 3$ for $A > 0.6\pi$. This figure is in excellent agreement with the study shown in [13], where analytic and simulated results are shown, suggesting that this new simulator is working and producing the expected results for thick αL.

While work had been done on the data storage sequence, there has been no discussion of the power efficiencies for TTD sequences. As was stated in chapter 2, TTD can be created using brief pulses or with chirped pulses. Figure 17 (b) shows an example of programming TTD using brief pulses. Now, two brief pulses, of significant pulse areas $\Theta_1 = \Theta_2$, write a spectral grating into the medium, then an arbitrary data pulse, with a low pulse area Θ_p and low bandwidth compared to the brief pulses, probes the grating, stimulating a TTD version of itself.

The power efficiencies for the brief pulse TTD programming sequence are shown in figure 19. In this simulation, $\Theta_1 = \Theta_2 = A$ and range from 0.1 to 0.9 π. The first and second pulses were Guassian with FWHM's of 0.1 ns. The data pulse was also Guassian and had a FWHM of 0.2 ns and $\Theta_P = 0.05\ \pi$. It can be seen in this figure that the echo efficiency peaks around an $\alpha L = 2.3$, with a maximum efficiency of 33% for A = 0.5π. This is a significant efficiency, compared to thin αL's where efficiencies of 0.1-2% are common. Thus, as previously demonstrated for the programming